MATRIX ISOLATION RESONANCE RAMAN AND CAVITY RINGDOWN SPECTROSCOPY OF SPECIES OF ASTROPHYSICAL INTEREST

BY

JASON FRANK FULLER

A DISSERTATION PRESENTED TO THE GRADUATE SCHOOL
OF THE UNIVERSITY OF FLORIDA IN PARTIAL FULFILLMENT
OF THE REQUIREMENTS FOR THE DEGREE OF
DOCTOR OF PHILOSOPHY

UNIVERSITY OF FLORIDA

2001

ACKNOWLEDGMENTS

There are several people that allowed this dissertation to be a reality. I would like to begin by thanking Dr. Jan Szczepanski for his guidance on numerous topics during my time here at the University of Florida and for his constant willingness to share his wisdom and experience. I would also like to thank Dr. Martin Vala, who has been essential in the furthering of my education and the maneuvering through the dissertation process. While I was at the University of Florida, Drs. Sam Colgate and Mike Zerner showed me how to convey knowledge in both an exciting and effective manner. I also thank the staff of the machine shop, especially Mr. Todd Prox, for their instruction and guidance.

I also acknowledge the support of my family. My parents, Pat and Frank Fuller, encouraged me from an early age. They instilled in me the belief that there was no accomplishment too great to achieve, both by their encouragement and example. Finally, I thank my wife, Renee, for her unending love and encouragement. Without Renee's support and understanding the completion of this dissertation would not have been possible.

TABLE OF CONTENTS

page

ACKNOWLEDGMENTS ii

ABSTRACT v

CHAPTERS

1 INTRODUCTION 1
Astrophysical Background 1
The Interstellar Medium 1
Carbon-Bearing Species in the Interstellar Medium 2
Unidentified Interstellar Absorptions and Emissions 3
Experimental Methods 6
Matrix Isolation Spectroscopy 6
Pulsed Molecular Jet Spectroscopy 7

2 RESONANCE RAMAN SPECTROSCOPY OF ODD-NUMBERED LINEAR CARBON CLUSTERS C_{15} to C_{23} 9
Introduction 9
Background 10
Experimental and Computational Procedures 15
Experimental Procedures and Apparatus 15
Theoretical Methods 15
Results 17
Experimental Resonance Raman Spectra 17
Theoretical 18
Discussion 25
Summary 34

3 CAVITY RINGDOWN SPECTROSCOPY 36
Introduction 36
Cavity Ringdown Apparatus 40
Optical Cavity 40
Laser System 43
Triggering and Measurement of a Ringdown Transient 46
Molecular Beam and Pulsed Discharge Sources 46
Experimental 49
Cavity Ringdown Absorption of Molecular Oxygen 49
Cavity Ringdown Absorption on Azulene 51
Cavity Ringdown Absorption of Naphthalene Cation 52
Results and Discussion 52
The 2-0 Band of the Red Bands of Oxygen 52
The S_1-S_0 Absorption of Azulene 57

The D_2-D_0 Absorption of Naphthalene Cation 57
Summary 64

4 RED RECTANGLE BANDS AND C_3 65
Background 65
Future Experiments to Measure Gas-Phase C_3 Phosphorescence 69

5 SUMMARY 73

APPENDIX 75

REFERENCES 77

BIOGRAPHICAL SKETCH 83

Abstract of Dissertation Presented to the Graduate School
of the University of Florida in Partial Fulfillment of the
Requirements for the Degree of Doctor of Philosophy

MATRIX ISOLATION RESONANCE RAMAN AND CAVITY RINGDOWN SPECTROSCOPY OF SPECIES OF ASTROPHYSICAL INTEREST

By

Jason Frank Fuller

August 2001

Chair: Martin T. Vala
Major Department: Chemistry

Carbon clusters and ionized polycyclic aromatic hydrocarbons have generated much interest in the fields of astrophysics and physical chemistry. It has been hypothesized that these species are responsible for the diffuse interstellar bands (DIBs). Two projects are the focus of this dissertation. The first is resonance Raman spectroscopy of matrix-isolated linear carbon clusters, and the second project is construction and operation of a cavity ringdown spectrometer.

In the first project, odd-numbered linear carbon clusters were produced by laser ablation of graphite and were trapped in solid Ar at 12 K. These clusters were then probed using resonance Raman spectroscopy. This was done to confirm previous empirical assignments of the $^1\Sigma_u$-$^1\Sigma_g$ electronic transitions of the respective clusters. The most intense Raman feature in all clusters was the lowest energy totally symmetric, σ_g, carbon-carbon stretch. Observed Raman frequencies were compared with density functional theory calculations at the B3LYP/6-311G* level of theory.

Cavity Ringdown Spectroscopy (CRDS), the focus of the second project, is a relatively new, high sensitivity direct absorption technique based on light trapped

between two high reflectivity mirrors. A CRDS instrument was constructed and tested to determine its effectiveness in measuring electronic spectra of transient species. The testing phase involved measuring the doubly forbidden $^1\Sigma_u$-$^3\Sigma_g$ transition in oxygen and the S_1-S_0 transition of jet-cooled azulene. Finally the D_2-D_0 transition of the naphthalene cation, produced in a pulsed supersonic discharge, was measured, revealing two broad bands at 648.8 and 670.4 nm, which were compared to the DIBs.

CHAPTER 1
INTRODUCTION

Astrophysical Background

The Interstellar Medium

The "vacuum" of space in a misnomer. The space between the stars is filled with an extremely tenuous gas with an average density of only about one hydrogen atom per cm^3. This is the interstellar medium (ISM). However, our galaxy is vast, and despite its low density the ISM accounts for 20-30% or $\sim 10^{40}$ kg of the mass of our galaxy.[1,2] Much of this material has been ejected by old and dying stars. The ISM is not just the debris left over from star formation. It is a dynamical system, in which new stars continually form from interstellar gas clouds. During their lifetime stars discharge both mass and energy back into the ISM. These effects can be seen in the distribution of the ISM, which resembles earthly wind-blown clouds.

The ISM is composed mainly of three types of clouds: cold atomic clouds, warm diffuse clouds and molecular clouds.[3] Cold atomic clouds are characterized by densities of 10-20 atoms/cm^3 and temperature of approximately 50 K. Warm diffuse clouds are characterized by densities of ~0.1 atoms/cm^3 and temperature of approximately 5000 K. Together these two types of clouds account for roughly half the mass of the ISM. The third type of cloud, molecular clouds, has a higher density, ranging from 10^3-10^4 atoms/cm^3, and has a temperature ranging from 10-30 K. Molecular clouds occupy a small fraction of space, <1%, but contribute about half the mass of the ISM.

Carbon-Bearing Species in the Interstellar Medium

Observers use spectroscopy to remotely probe the atomic and molecular make-up of cosmic materials and derive cosmic abundances. The cosmic abundance of elemental species is drastically nonuniform. The cosmos comprises over 92% hydrogen, 6% helium, 0.07% oxygen, 0.04% carbon and 0.009% nitrogen.[4] By comparing laboratory observations of absorption and emission spectra spanning from the uv to submillimeter frequencies with astrophysical data, 121 interstellar and circumstellar molecules have been identified.[1] Interestingly, more than 75% of these species are carbon-bearing molecules.

The complexity of carbon-bearing molecules detected in the ISM varies greatly. It ranges from simple diatomics (CO, CH^+, and C_2), to small polyatomic species (C_3, C_3O, C_2H_2, and $HCOCH_3$), to large unsaturated species (C_8H and $HC_{11}N$). The $HC_{11}N$ cluster is the largest confirmed species in the ISM to date.[5,6] Complex mechanisms have been developed to describe the formation of molecules and ions in different regions of space.[7-9] These mechanisms involve a combination of photo-ionization, gas phase ion-molecule, and dust-grain surface chemistry. The pathway for producing simple carbon-bearing molecules in diffuse clouds, where carbon atoms are primarily in the singly ionized state, C^+, begins with the radiative association reaction of C^+ with H_2 to yield CH_2^+, which in turn can react with H_2 to produce CH_3^+. The CH_3^+ then dissociatively combines with an electron to produce CH_2 and CH. The reaction of these neutrals with C^+ leads to the formation of longer carbon clusters. However, this mechanism is limited by uv photodissociation of neutral species at the surface to intermediate depths within the diffuse cloud. In dense clouds, carbon atoms are shielded from uv photons and are mostly neutral. In this case the initial reaction in the

mechanism is $C + H_3^+$, which produces CH_3^+. Complex carbon-bearing molecules are then formed by carbon atom insertion, condensation and radiative association reactions.

Unidentified Interstellar Absorptions and Emissions

In addition to the confirmed interstellar and circumstellar species, there remains a ubiquitous set of absorption and emission features that have not been assigned carriers. These unidentified features are the diffuse interstellar absorption bands (DIBs), the unidentified interstellar infrared (UIR) emission bands, and the Red Rectangle emission bands (RRBs).

Diffuse interstellar absorption bands. The diffuse interstellar bands are absorption features superimposed on the interstellar extinction curve throughout the visible and near infrared spectral range. The DIBs have been shown to be of interstellar origin by Merrill over 75 years ago.[10,11] These bands are observed in a spectral range extending from 400-1300 nm, and are notable for their lack of any recognizable pattern, apart from an apparent progression with a ~35 cm^{-1} spacing observed by Herbig.[12] Additionally, the DIBs show a strong variation of band profiles (FWHM range from 0.8-30 Å).[13] Presently more than 250 DIBs are known.[14] Figure 1-1 shows the synthetic DIB spectrum of the hot star BD+63 1964.[14,15] There have been many suggestions as to the species responsible for the DIBs. Laboratory observations point to polycyclic aromatic hydrocarbons (PAHs),[16,17] carbon clusters or chains,[18,19] and carbon rings or fullerenes[20,21] as potential carriers for some of the DIBs. Homologous series of odd-numbered C_n clusters have also been suggested as carriers of the DIBs.[22] However, the abundance of carbon clusters in the diffuse medium is estimated to be very low, ~10^{-10}/H atom. This is about 10^3 times lower than the estimated PAH concentration, which strongly suggests a limited contribution from carbon clusters to the DIB spectrum.[23,24] Worthy of further investigation is the hypotheses that long clusters are responsible for some DIBs, as they

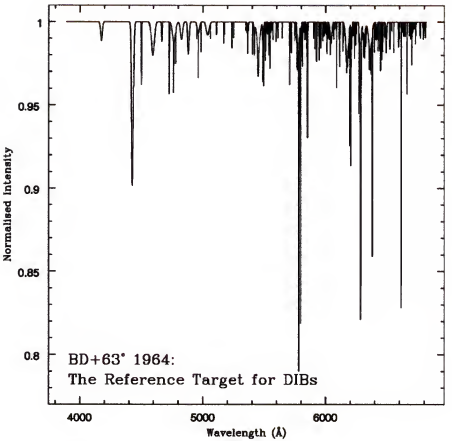

Figure 1-1. The synthetic spectrum of the hot BOII star BD + 63 1964.[14,15] This object is currently used as a reference target of diffuse bands, displaying more than 250 DIBs in the range 3900–7000 Å and a significant enhancement of narrow DIBs.

have electronic transitions in the visible. At present, no definitive identification of the carriers of any of the 250 bands exists. Spectroscopic observations of species trapped in rare gas matrices can point to possible carriers, but spectroscopic observations in the gas phase are needed for definitive identification.

Unidentified interstellar infrared emission bands. Discovered in 1973, the unidentified interstellar infrared (UIR) emission bands are a series of overlapping bands between 3.3 and 11.3 μm, that have been observed in a variety of interstellar environments.[25,26] Figure 1-2 shows the infrared spectra of various objects in the ISM.[27] It has been proposed that the bands originate from neutral and/or ionic PAHs.[28,29] Although there now exists evidence in support of this hypothesis, the exact mixture of

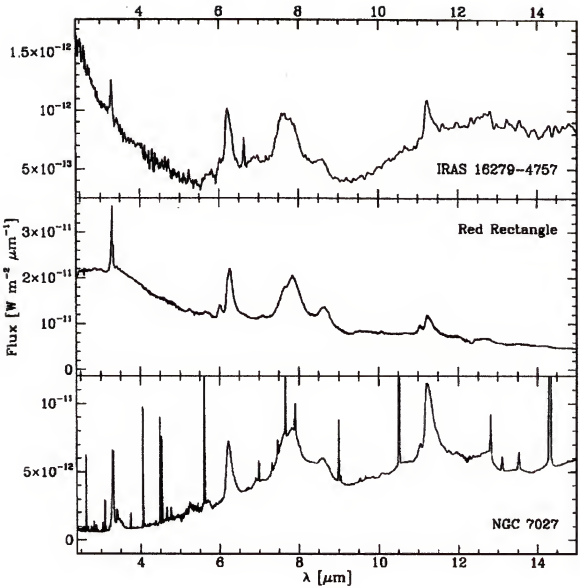

Figure 1-2. Emission spectra in the 3–15 μm range of the post Asymptotic Giant Branch objects,[27] IRAS 16279-4757, the Red Rectangle, and the planetary nebula NGC 7027. The different objects display a rich and variable spectrum of infrared emission bands.

PAHs, their relative stability, their state of ionization, their degree of dehydrogenation, and their propensity to aggregate are still a matter of active debate among researchers.[30-32]

In this dissertation matrix-isolation resonance Raman and cavity ringdown spectroscopy are used to study carbon-bearing molecules in order to gain a better understanding of their chemical and physical properties and of their role in the ISM.

Experimental Methods

Many of the interesting molecular and ionic species studied spectroscopically are transient species that require some manner of isolation to prevent unwanted reactions. Two widely used techniques for isolating and studying such species are matrix isolation spectroscopy, for condensed phase experiments, and molecular jet spectroscopy, for gas phase experiments.

Matrix Isolation Spectroscopy

Matrix isolation spectroscopy was first demonstrated by Whittle, Dows, and Pimentel in 1954,[33] and since then numerous books and articles have been published on the subject.[34,35] Essentially this technique involves the codeposition, at cryogenic temperatures, of the matrix gas with the gas-phase species of interest. The sample is trapped in the rigid matrix preventing diffusion, thus precluding unwanted reactions with other trapped species. However, in some instances, diffusion of species within the matrix is desired, to allow reactions, and the matrix may be annealed to facilitate this process. The temperature needed to form a rigid matrix should not exceed approximately one-third of the melting point of the matrix gas (for example, 8 K for neon and 27 K for argon). When choosing a matrix gas, two criteria must be considered. Most importantly the matrix gas must be spectroscopically transparent in the electromagnetic energy region to be studied. Second, the matrix gas must be as weakly interacting as possible. In practice, few materials other than the rare gases and molecular nitrogen are chemically inert enough to serve as a matrix for the most reactive

species, and the rare gases are primarily used since they are transparent from the vacuum uv to the far infrared.

Matrix isolation spectroscopy appears to be the ideal method for studying reactive species; however, this technique is not without its limitations. Matrix isolated species are not completely free of intermolecular and guest/host interactions. The magnitude of these interactions is far less than in the bulk solid or liquid (if applicable). It is usually possible to consider matrix effects as a perturbation of the property being studied, and the observed spectroscopic property may be taken as representative of those of the free molecule or ion. Matrix perturbations generally manifest themselves as some combination of line broadening, band splitting, and the matrix-to-gas phase frequency shift. In this dissertation matrix isolation is employed to study resonance Raman spectroscopy of linear carbon clusters.

Pulsed Molecular Jet Spectroscopy

Pulsed molecular jet spectroscopy is used to probe gas phase species. This method evolved from effusive beam techniques and has been in use for over half a century. Numerous books have been written on molecular jet and beam spectroscopy.[4,36,37] In a molecular jet the species to be studied is seeded in a carrier gas, usually helium or argon, at a pressure of 2-3 atm and expanded through a small diameter nozzle (d~1 mm) into a vacuum. As the gas expands through the nozzle, adiabatic cooling occurs, whereby the thermal energy of the molecules is converted to directed kinetic energy along the axis of expansion. This process is represented in Figure 1-3. In the region of the nozzle, energy is exchanged among the molecules by collisions, resulting in translational cooling along with an increase in velocity in the direction of the expansion. The seeded species then gives up rotational and vibrational energy to the cold carrier gas through collisions. The degree of cooling depends upon

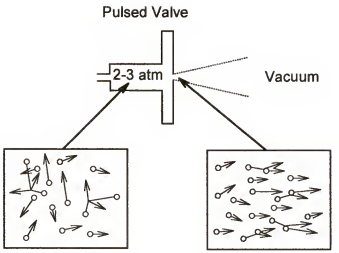

Figure 1-3. Cartoon representing the adiabatic expansion of molecules in a supersonic molecular jet. The molecules are cooled by allowing them to pulse out of the nozzle. The arrows represent velocity vectors.

the interaction cross-section for collisions with exchange of rotational and vibrational energy. This is a function of the pressure differential during the expansion and the frequency and width of the applied pulse. In general, the effective temperature ranges are as follows: $T_{translational}$ ~1-20 K, $T_{rotational}$ ~2-50 K, and $T_{vibrational}$ ~10-100K. At such low effective rotational and translational temperatures, only the lowest ro-vibrational levels in the electronic ground state are populated. This significantly reduces the number of possible initial states for absorptive transitions and thus the number of lines in the spectrum.

The two most widely used pulsed valve designs are the Gentry-Giese high speed valves[38,39] (10-100 ms pulse width, 1-10 Hz) which use pulsed currents to open and close a hairpin type valve and solenoid valve systems[40,41] (10-100 ms pulse width, 35-100 Hz) that pulse a ferromagnetic plunger and poppet assembly. In this study, a solenoid valve system is used to study the electronic absorption of two PAHs, which are probed using cavity ringdown spectroscopy.

CHAPTER 2
RESONANCE RAMAN SPECTROSCOPY OF ODD NUMBERED LINEAR CARBON CLUSTERS C_{15}-C_{23}

Introduction

Much progress has been made in understanding the structure and properties of pure carbon clusters.[42,43] Despite this increased knowledge, much information concerning carbon clusters remains unexplored or unknown. This includes the limited experimental measurements of large neutral carbon clusters, and the role of carbon clusters as carriers of the diffuse interstellar absorption bands (DIB) and the unidentified interstellar infrared (UIR) emission bands. Measurements from infrared[44-46] and Raman spectroscopy[47] are available for smaller neutral carbon clusters. However, experimental measurements on clusters larger than C_{13} remain scarce. Furthermore there is little information on symmetric stretching mode frequencies of any size carbon cluster. Symmetric stretching frequencies of linear carbon clusters have been measured by photoelectron spectroscopy,[48,49] Raman spectroscopy,[50,51] and by extraction from infrared combination bands.[52]

Additionally, questions arise concerning carbon clusters as carriers of the DIBs and UIR bands. In 1996 Onaka and coworkers[53] discovered that the UIR bands could be observed in regions of space that had until then only exhibited absorption in the visible spectrum (i.e., the DIBs). In 1977 Douglas proposed that long chain carbon clusters (C_n, n=5-15) could be responsible for the DIBs,[54] but later Leger and d'Hendecourt[55] calculated that most carbon clusters of this size would be photodissociated in the interstellar medium. However, recently Maier and coworkers[56]

were able to match four of the DIBs with absorption bands in C_7^-, but rigorous comparisons with astrophysical observations[57,58] raised questions about the assignment of C_7^- as a carrier of the DIBs. Herbst and coworkers[59] also raised questions concerning the origin and long-term stability of this species. Despite these criticisms, the excellent match allows for the possibility that carbon chain molecules could contribute to the interstellar spectral bands. Definitive answers must await gas-phase measurements.

In this study, the resonance Raman spectra of matrix isolated C_{15}, C_{17}, C_{19}, C_{21}, and C_{23} clusters were recorded to provide supporting evidence for the assignment of the 0-0 electronic absorption of neutral linear carbon clusters. The experimental resonance Raman frequencies were also compared with density functional theoretical (DFT) vibrational frequencies. The odd-numbered cluster Raman frequencies are compared with even-numbered cluster Raman frequencies observed by Jarrold and coworkers.[50,51]

Background

Electronic absorption spectra of neutral linear carbon clusters trapped in rare gas matrices have been observed for species as large as C_{21}. Early work by Weltner and McLeod[60] focused on C_2 and C_3; however, they observed other absorptions in the ultra violet and visible (uv/vis) regions after matrix annealing. These bands were attributed to larger carbon species (n>3). About 20 years later, Kratschmer and coworkers[61] measured the uv/vis absorption of matrix isolated carbon clusters and tentatively assigned the prominent absorption features to species spanning the range from C_4 to C_9. More recently Maier and coworkers measured the electronic absorption spectrum of mass-selected carbon clusters, C_n (n=6-14, even)[62] and C_n (n=5-15, odd).[63] Maier's research group has also observed the electronic absorption of odd numbered species, C_{17}-C_{21}, produced by laser ablation of graphite and trapped in neon with no mass selection.

In the mass selection experiments from Maier's group, a monotonic decrease in energy of the $^1\Sigma_u - {}^1\Sigma_g$ transition with increasing number of carbon atoms was observed for C_n (n=5-15, odd).[63] This observation established a linear relation between the energy of the 0-0 transition and the number of carbon atoms in the linear cluster for odd numbered species. This is indicative of a homologous series and can be rationalized by a HOMO-LUMO, π-π^* transition within the particle-in-a-box model.

In later experiments Maier and coworkers[64] measured the electronic absorption of carbon clusters formed by laser ablation and deposited (without mass selection) in a neon matrix. In these experiments additional carbon cluster absorption features were observed that fit on the extrapolated linear plot from their mass selection experiments. On this basis, the new absorption bands were assigned to C_{17}, C_{19}, and C_{21}.

Work in our lab produced the visible absorption spectrum for laser-ablated graphite deposited in an argon matrix at 20 K. This spectrum is shown in Figure 2-1. The lower trace is recorded directly after deposition at 20 K while the upper trace is after annealing to 36 K. The upper trace is similar to that of Maier and coworkers for C_n species in a neon matrix annealed to 9 K. Table 2-1 compares the band positions in a neon matrix to those in an argon matrix. The wavelength spacing for adjacent clusters is slightly larger in argon compared to neon (~46 nm/C_2 in argon and ~41 nm/C_2 in neon). Figure 2-2 shows the plot of the 0-0 transition energy in nm as a function of chain length, n, and the linear fit for n=11-21. The equation of the linear fit is λ(nm) = 23.20n +97.95, where n is the number of carbon atoms in the odd-numbered chain. If the linear fit is extended to longer wavelength, to encompass clusters larger than C_{21}, the absorption bands in Figure 2-1 at 633.5, 678.0, ~725, and 768.0 nm are seen to also fit well on the linear plot. Therefore, these bands are tentatively assigned to the larger linear clusters, C_{23}, C_{25}, C_{27}, and C_{29}, respectively. If the linear fit is extended to shorter wavelength, it

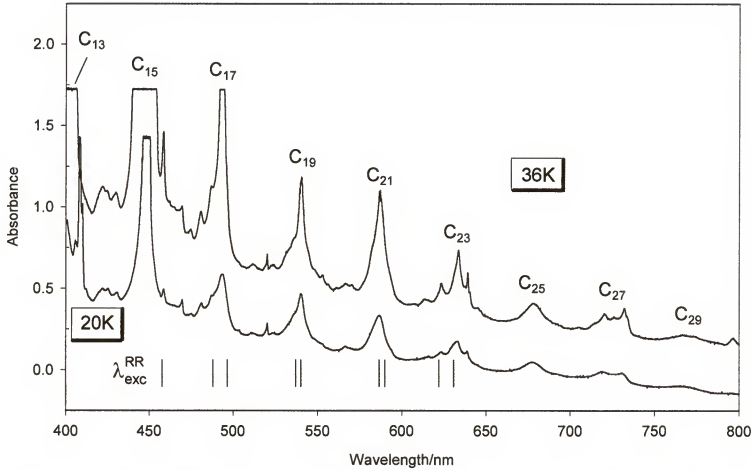

Figure 2-1. Electronic absorption spectra for certain C_n clusters formed by laser ablation of graphite and deposited in an Ar matrix at 20 K (lower trace) and after annealing to 36 K, and recooling to 20 K (upper trace). Resonance Raman excitation wavelengths are labeled by vertical lines.

Table 2-1. Experimental and predicted absorption bands of $^1\Sigma_u - {}^1\Sigma_g$ transition for odd numbered linear C_{11}-C_{29} carbon clusters observed in Ne and Ar matrices.

Ne matrix, 6 K[a]			Ar matrix, 36 K[b]				
λ/nm	ν/cm^{-1}	Δλ/nm	λ/nm	ν/cm^{-1}	Δλ/nm	Predicted/nm[c]	Assignment
			~168.0[a]	59524	(0.0)	167.6	C_3
			189.0[d]	52910	0.0		C_3
			226.1	44228	37.1	214.0	C_5
252.8	39556	0.0				260.4	C_7
295.0	33895	42.2	307.9[e]	32478	81.8	306.8	C_9
336.3	29732	41.3	354.0	28249	46.1	353.2	C_{11}
379.6	26341	43.3	400.5	24969	46.5	399.6	C_{13}
419.6	23832	40.0	447.0	22371	46.5	446.0	C_{15}
460.3[f]	21719	40.7	493.0	20284	46.0	492.4	C_{17}
503.2[f]	19867	42.9	539.2	18546	46.2	538.8	C_{19}
543.7[f]	18387	40.5	586.4	17053	47.2	585.2	C_{21}
			633.5	15785	47.1	631.6	C_{23}
			678.0	14749	44.5	678.0	C_{25}
			725.9	13776	47.9	724.4	C_{27}
			768.0	13021	42.1	770.8	C_{29}

[a] Ref. 63
[b] This work and Ref. 65
[c] From linear fit, see text
[d] Ref. 66
[e] Ref. 67,68
[f] Ref. 64

is possible to predict the 0-0 band head positions for smaller clusters, i.e. n=3-11. The following positions are predicted: 167.6 (C_3), 214.0 (C_5), 260.4 (C_7), 306.8 (C_9), and 353.2 (C_{11}) nm for the odd clusters C_n, n=3-11, respectively. A comparison of the observed bands with these predictions, as in Table 2-1, offers support for the linear relation between the wavelength of the 0-0 transition and chain length. Since the extension of the linear plot to longer chains is just an empirical fit, resonance Raman spectroscopy was used to confirm the long carbon chain assignments.

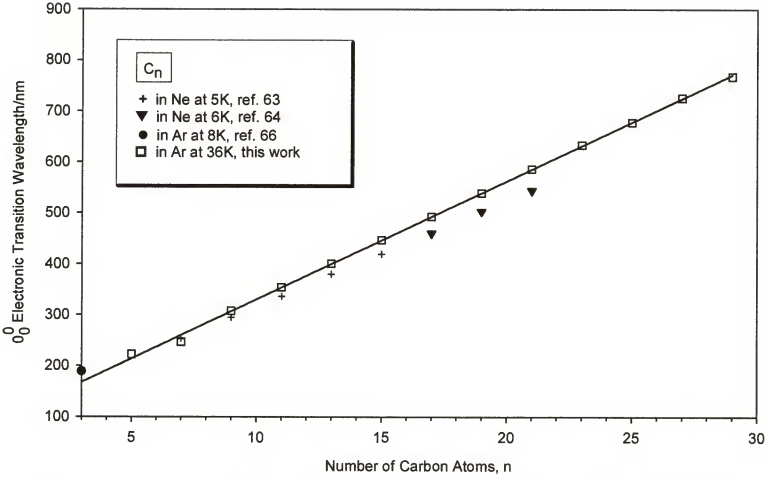

Figure 2-2. Plot of the $^1\Sigma_u$-$X^1\Sigma_g$ transition wavelength for odd-numbered linear carbon clusters as a function of number of carbon atoms in the chain.

Experimental and Computational Procedures

Experimental Procedures and Apparatus

A diagram of the apparatus used to measure the resonance Raman spectra of linear carbon clusters is shown in Figure 2-3. Neutral carbon clusters were produced by laser ablation of a graphite rod using a Q-switched Nd:YAG laser (1064/532 nm, 10 Hz, 20-50 mJ). The gaseous reaction products were mixed with Ar and trapped on an aluminum or silver-coated copper cold finger cooled to 12 K by a closed cycle helium cryostat (ADP Displex). To provide freshly vaporized carbon material, the laser beam was displaced across the graphite surface by an oscillating lens. Reaction products were probably formed at the vaporization point, while landing on the matrix surface, and during matrix annealing. The matrices were annealed by two methods. The first allowed the matrix to warm to 35 K by cutting power to the cryostat. The matrix was then re-cooled 12 K. The second method used a temperature controller to warm the matrix to 35 K. This temperature was maintained for 10 to 15 minutes before re-cooling. Excitation in the resonance Raman (RR) work was effected with the 456, 488, and 496.5 nm lines of an Ar^+ laser (Spectra Physics model 164) and various wavelengths from a dye laser (with Coumarin 540, Rhodamine 590 and Rhodamine 610 dyes) pumped by an Ar^+ laser. The RR spectra were scanned with a Spex 1401 double monochromator and were detected using photon counting. To record absorption spectra, the ablation products were trapped on a BaF_2 cryostat window held at 20 K. Absorption spectra were recorded in the 400-800 nm range using a Cary 17 UV-visible spectrometer.

Theoretical Methods

Optimized geometries and harmonic vibrational frequencies were calculated using Gaussian 98, Revision A.6.[69] The vibrational properties were calculated using

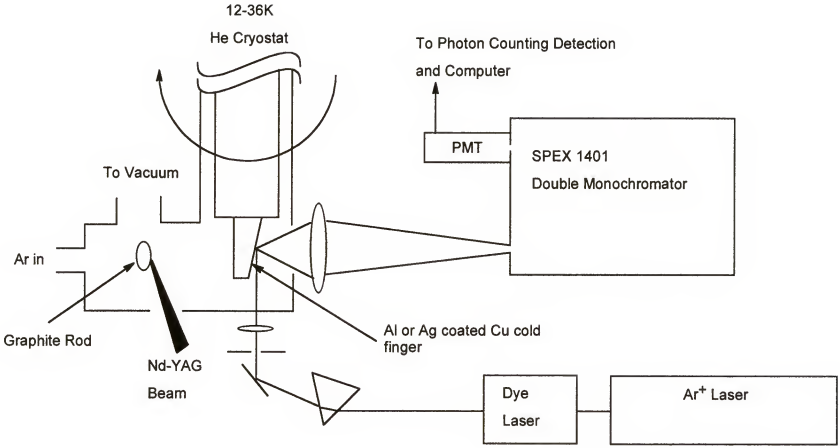

Figure 2-3. Resonance Raman spectrometer

density functional theory with the B3LYP (Becke three-parameter-Lee-Yang-Parr) functional[70] and the 6-311G* basis set. The computed frequencies were uniformly scaled by 0.95 to correct for anharmonicity.

Results

Experimental Resonance Raman Spectra

The resonance Raman (RR) spectra of linear odd-numbered carbon clusters C_n (n=15-23) are shown in Figures 2-4 through 2-8. The excitation wavelengths for each cluster were chosen to be within the absorption band envelope of that cluster (cf. Figure 2-1). The excitation wavelengths used for each cluster are given in below in Table 2-2.

Table 2-2. Excitation laser parameters for resonance Raman spectra.

Cluster	λ_{exc}/nm	Power/mW
C_{15}	457.9	20
C_{17}	488.0	10
	496.5	20
C_{19}	536.9	10
	540.0	20
C_{21}	586.4	100
	589.7	100
C_{23}	622.0	50
	630.7	50

For all clusters at least two laser excitation lines were used, except for C_{15} where only one was possible in its shorter wavelength absorption region. No apparent fluorescence was observed for any cluster. The experimental RR frequencies and assignments are listed in Table 2-3. The RR excitation profile for C_{21} was constructed and is shown in Figure 2-9.

Table 2-3. Experimental resonance Raman frequencies for odd number carbon clusters C_{15}-C_{23}.

C_{15} Raman shift/cm^{-1}	C_{17} Raman shift/cm^{-1}	C_{19} Raman shift/cm^{-1}	C_{21} Raman shift/cm^{-1}	C_{23} Raman shift/cm^{-1}
111	135	197	136	173
141	220	214	192	208
219	237	237	217	246
267	254	266	268	270
309	268	311	333	316
367	342	371	381	331
437	472	425	469	350
533	500	447	490	381
659	534	475	536	474
739	648	490	578	494
789	698	577	586	524
919	738	627	622	538
993	794	649	655	564
1035	868	781	731	596
1056	962	853	773	656
1137	990	903	839	766
1209	1459	937	891	804
1259	1034	963	924	959
1324	1138	987	962	990
1424	1600	1045	997	1698
1457	1638	1589	1174	1758
1511	1944	1823	1269	1850
1639	1962	1851	1759	1960
1847	2112	1869	1822	
1921		1917	1849	
1933		1951		
1959				
2035				

Theoretical

Density functional theory calculations (B3LYP/6-311G*) have been performed to determine the geometries and vibrational frequencies for C_n (odd, n=15-23). Both Raman and infrared frequencies are given for these clusters in Tables 2-4 through 2-8.

The total number of vibrations for a linear carbon cluster, C_n ($D_{\infty h}$), is 3n-5. Of this total number of vibrations, there are two types of normal modes: longitudinal, in

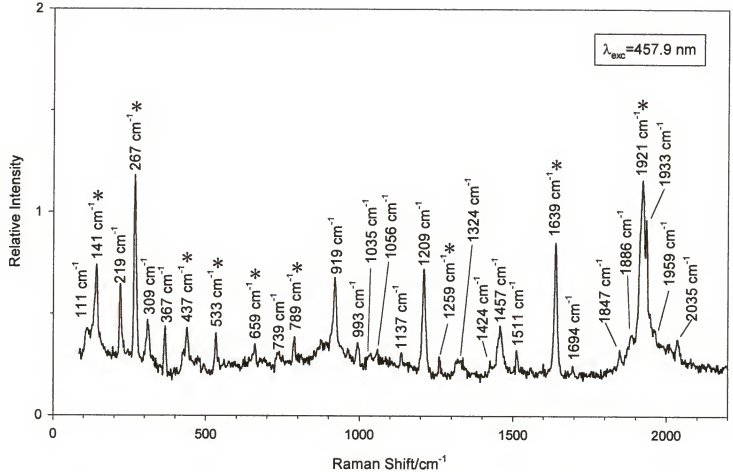

Figure 2-4. Resonance Raman spectrum of linear C_{15} in an Ar matrix at 12 K. The excitation wavelength was 457.9 nm, and the laser power was 20 mW. Assigned bands are designated with *.

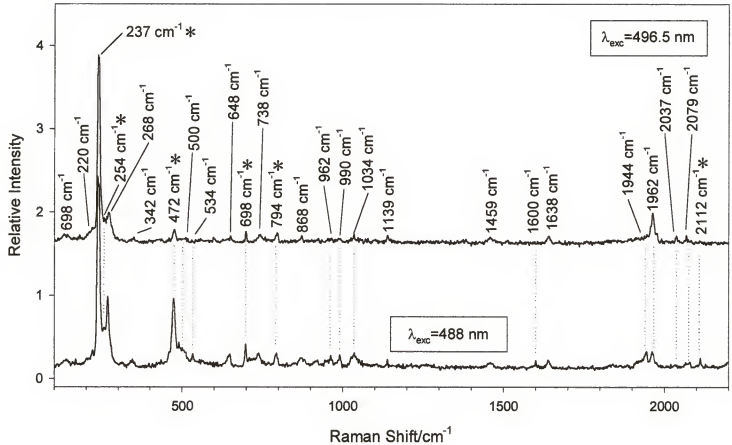

Figure 2-5. Resonance Raman specta of linear C_{17} in an Ar matrix at 12 K. In the upper trace the excitation wavelength was 496.5 nm, and the laser power was 10 mW. In the lower trace the excitation wavelength was 488 nm, and the laser power was 10 mW. Assigned bands are designated with *.

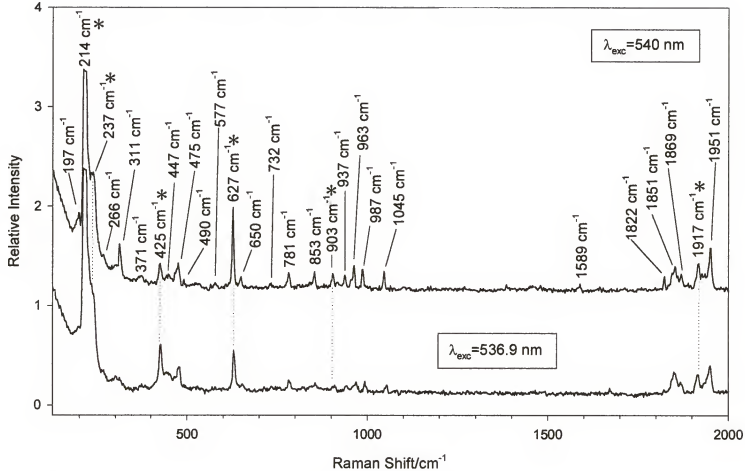

Figure 2-6. Resonance Raman spectra of linear C_{19} in an Ar matrix at 12 K. In the upper trace the excitation wavelength was 540 nm, and the laser power was 10 mW. In the lower trace the excitation wavelength was 536.9 nm, and the laser power was <10 mW. Assigned bands are designated with *.

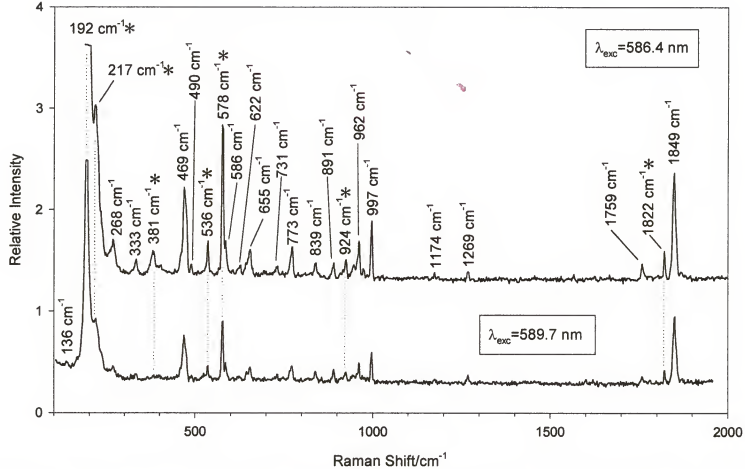

Figure 2-7. Resonance Raman spectra of linear C_{21} in an Ar matrix at 12 K. In the upper trace the excitation wavelength was 586.4 nm, and the laser power was 100 mW. In the lower trace the excitation wavelength was 589.7 nm, and the laser power was 100 mW. Assigned bands are designated with *.

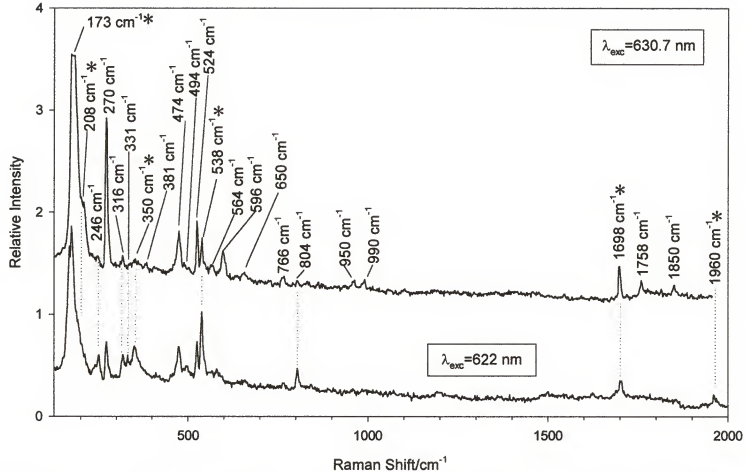

Figure 2-8. Resonance Raman spectra of linear C_{23} in an Ar matrix at 12 K. In the upper trace the excitation wavelength was 630.7 nm, and the laser power was 50 mW. In the lower trace the excitation wavelength was 622 nm, and the laser power was 50 mW. Assigned bands are designated with *.

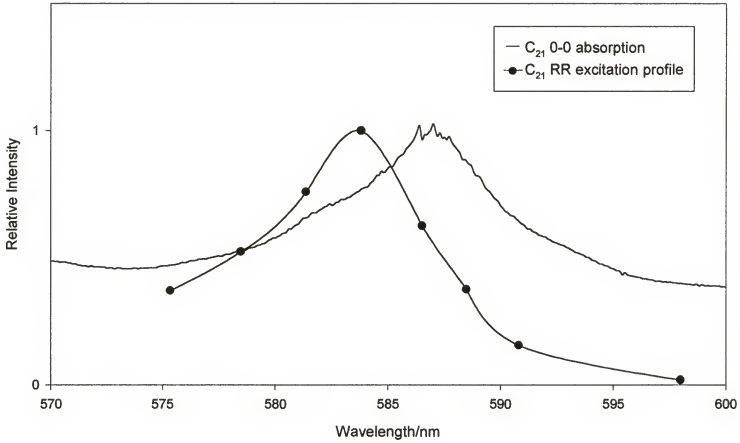

Figure 2-9. Resonance Raman excitation profile for 192 cm^{-1} band of C_{21} superimposed on the 0-0 absorption band. The ● are RR excitation wavelengths.

which the carbon atoms undergo longitudinal displacements along the molecular axis and transverse, in which the carbon atoms are displaced perpendicularly to the molecular axis. Using group theory it is possible to determine the number and character of these normal modes. For a molecule containing an odd number of atoms, n, of $D_{\infty h}$ symmetry, there are (n-1)/2 normal vibrational modes of σ_g^+ symmetry and (n-1)/2 of σ_u^+ symmetry (these are longitudinal modes) and (n-3)/2 doubly degenerate normal vibrational modes of π_g symmetry and (n-1)/2 of π_u symmetry (these are transverse modes).[71,72]

Discussion

The observed and specific calculated RR frequencies and their assignments for odd-numbered clusters C_{15}-C_{23} are given in Table 2-9. Of particular interest is the observation of the most intense band, which for all five clusters is the lowest energy σ_g mode. The frequencies of these σ_g modes decrease with increasing chain length: 267 cm^{-1} (C_{15}), 237 cm^{-1} (C_{17}), 214 cm^{-1} (C_{19}), 192 cm^{-1} (C_{21}), 173 cm^{-1} (C_{23}). These values interleave well with the Raman observations of Jarrold and Van Duyne and coworkers[50,51] for mass-selected C_n clusters (even, n=14-20) deposited in N_2 matrices. These Raman frequencies are listed, together with the RR frequencies from this study, in Table 2-10, and are labeled Series I. Table 2-10 also lists the next lowest energy σ_g mode (Series II). These bands are often the second most intense and also decrease in energy with increasing chain length. Series I and II frequencies are plotted versus chain length in Figure 2-10 and can be seen to fall on smooth curves. These two series are totally symmetric carbon-carbon stretching modes as seen in Figure 2-11. The lower frequency series (I) can be described as the equal amplitude and out-of-phase motion of carbon atoms in one half of the cluster with their analogs in the other half. The higher

Table 2-4. Linear C_{15}: optimized geometry and calculated frequencies at the B3LYP/6-311G* level.

Geometry[a]: 1.2846, 1.2917, 1.2676, 1.2803, 1.2716, 1.2771, 1.2745Å

C_{15} calculated vibrational frequencies/cm^{-1} [b]	vibrational mode	intensity/$km \cdot mol^{-1}$
2122.1	ν_1, σ_g	
2094.7	ν_2, σ_g	
1944.1	ν_3, σ_g	
1658.4	ν_4, σ_g	
1235.9	ν_5, σ_g	
772.8	ν_6, σ_g	
266.1	ν_7, σ_g	
2137.9	ν_8, σ_u	2750
2050.3	ν_9, σ_u	620
1884.6	ν_{10}, σ_u	27413
1819.2	ν_{11}, σ_u	8777
1450.2	ν_{12}, σ_u	290
1009.8	ν_{13}, σ_u	9
524.8	ν_{14}, σ_u	18
678.1	ν_{15}, π_g	
521.0	ν_{16}, π_g	
424.2	ν_{17}, π_g	
244.4	ν_{18}, π_g	
138.2	ν_{19}, π_g	
48.0	ν_{20}, π_g	
660.0	ν_{21}, π_u	13
520.2	ν_{22}, π_u	1
473.6	ν_{23}, π_u	1
286.6	ν_{24}, π_u	1
189.0	ν_{25}, π_u	5
89.6	ν_{26}, π_u	6
17.7	ν_{27}, π_u	3

[a] Bond lengths starting at terminal carbon

[b] Frequencies scaled by 0.95

Table 2-5. Linear C_{17}: optimized geometry and calculated frequencies at the B3LYP/6-311G* level.

Geometry[a]: 1.2843, 1.2924, 1.2672, 1.2811, 1.2710, 1.2781, 1.2736, 1.2759Å

C_{17} calculated vibrational frequencies/cm^{-1} [b]	vibrational mode	intensity/$km \cdot mol^{-1}$
2135.7	ν_1, σ_g	
2062.0	ν_2, σ_g	
2020.2	ν_3, σ_g	
1820.9	ν_4, σ_g	
1489.4	ν_5, σ_g	
1106.4	ν_6, σ_g	
687.4	ν_7, σ_g	
235.0	ν_8, σ_g	
2125.8	ν_9, σ_u	3104
2093.7	ν_{10}, σ_u	2772
1927.9	ν_{11}, σ_u	2
1815.9	ν_{12}, σ_u	46977
1670.0	ν_{13}, σ_u	1729
1302.6	ν_{14}, σ_u	141
901.2	ν_{15}, σ_u	0
465.0	ν_{16}, σ_u	25
790.9	ν_{17}, π_g	
563.0	ν_{18}, π_g	
469.0	ν_{19}, π_g	
298.3	ν_{20}, π_g	
205.6	ν_{21}, π_g	
113.1	ν_{22}, π_g	
38.1	ν_{23}, π_g	
777.1	ν_{24}, π_u	11
549.7	ν_{25}, π_u	0
499.0	ν_{26}, π_u	3
416.1	ν_{27}, π_u	0
256.7	ν_{28}, π_u	2
159.2	ν_{29}, π_u	6
71.9	ν_{30}, π_u	5
13.9	ν_{31}, π_u	3

[a] Bond lengths starting at terminal carbon
[b] Frequencies scaled by 0.95

Table 2-6. Linear C_{19}: optimized geometry and calculated frequencies at the B3LYP/6-311G* level.

Geometry[a]: 1.2841, 1.2929, 1.2668, 1.2818, 1.2705, 1.2789, 1.2730, 1.2769, 1.2750Å

C_{19} calculated vibrational frequencies/cm^{-1} [b]	vibrational mode	intensity/km·mol^{-1}
2136.4	ν_1,σ_g	
2075.9	ν_2,σ_g	
2019.1	ν_3,σ_g	
1908.6	ν_4,σ_g	
1681.9	ν_5,σ_g	
1354.8	ν_6,σ_g	
1000.9	ν_7,σ_g	
618.5	ν_8,σ_g	
210.4	ν_9,σ_g	
2122.3	ν_{10},σ_u	278
2101.1	ν_{11},σ_u	7880
2000.3	ν_{12},σ_u	1336
1819.6	ν_{13},σ_u	1125
1755.8	ν_{14},σ_u	61416
1518.9	ν_{15},σ_u	628
1181.6	ν_{16},σ_u	66
813.2	ν_{17},σ_u	1
417.2	ν_{18},σ_u	32
915.6	ν_{19},π_g	
618.1	ν_{20},π_g	
504.9	ν_{21},π_g	
416.8	ν_{22},π_g	
266.8	ν_{23},π_g	
176.4	ν_{24},π_g	
93.6	ν_{25},π_g	
30.8	ν_{26},π_g	
902.5	ν_{27},π_u	11
601.8	ν_{28},π_u	0
511.7	ν_{29},π_u	4
462.2	ν_{30},π_u	0
302.3	ν_{31},π_u	1
218.4	ν_{32},π_u	3
133.3	ν_{33},π_u	5
58.8	ν_{34},π_u	4
11.2	ν_{35},π_u	3

[a] Bond lengths starting at terminal carbon
[b] Frequencies scaled by 0.95

Table 2-7. Linear C_{21}: optimized geometry and calculated frequencies at the B3LYP/6-311G* level.

Geometry[a]: 1.2838, 1.2933, 1.2665, 1.2823, 1.2701, 1.2796, 1.2725, 1.2776, 1.2743, 1.2760Å

C_{21} calculated vibrational frequencies/cm^{-1} [b]	vibrational mode	intensity/$km \cdot mol^{-1}$
2128.5	ν_1, σ_g	
2104.8	ν_2, σ_g	
1992.2	ν_3, σ_g	
1970.9	ν_4, σ_g	
1811.0	ν_5, σ_g	
1543.4	ν_6, σ_g	
1241.8	ν_7, σ_g	
913.4	ν_8, σ_g	
561.9	ν_9, σ_g	
190.4	ν_{10}, σ_g	
2130.4	ν_{11}, σ_u	2017
2081.9	ν_{12}, σ_u	6024
2048.1	ν_{13}, σ_u	5232
1896.6	ν_{14}, σ_u	559
1710.0	ν_{15}, σ_u	54980
1683.7	ν_{16}, σ_u	24974
1396.0	ν_{17}, σ_u	338
1080.6	ν_{18}, σ_u	27
740.5	ν_{19}, σ_u	7
378.2	ν_{20}, σ_u	38
1023.7	ν_{21}, π_g	
681.4	ν_{22}, π_g	
539.9	ν_{23}, π_g	
459.0	ν_{24}, π_g	
311.2	ν_{25}, π_g	
230.4	ν_{26}, π_g	
150.8	ν_{27}, π_g	
78.4	ν_{28}, π_g	
25.4	ν_{29}, π_g	
1015.9	ν_{30}, π_u	9
667.0	ν_{31}, π_u	1
531.3	ν_{32}, π_u	4
490.8	ν_{33}, π_u	0
410.2	ν_{34}, π_u	0
275.2	ν_{35}, π_u	1
191.3	ν_{36}, π_u	4
112.9	ν_{37}, π_u	5
48.7	ν_{38}, π_u	4
9.2	ν_{39}, π_u	2

[a] Bond lengths starting at terminal carbon, [b] Frequencies scaled by 0.95

Table 2-8. Linear C_{23}: optimized geometry and calculated frequencies at the B3LYP/6-311G* level.

Geometry[a]: 1.2836, 1.2937, 1.2663, 1.2827, 1.2698, 1.2801, 1.272, 1.2783, 1.2737, 1.2767, 1.2753Å

C_{23} calculated vibrational frequencies/cm^{-1} [b]	vibrational mode	intensity/$km \cdot mol^{-1}$
2122.2	ν_1,σ_g	
2114.5	ν_2,σ_g	
2034.9	ν_3,σ_g	
1943.4	ν_4,σ_g	
1883.9	ν_5,σ_g	
1696.8	ν_6,σ_g	
1430.1	ν_7,σ_g	
1145.7	ν_8,σ_g	
839.6	ν_9,σ_g	
514.7	ν_{10},σ_g	
173.9	ν_{11},σ_g	
2130.9	ν_{12},σ_u	3152
2089.5	ν_{13},σ_u	313
2049.1	ν_{14},σ_u	13146
1964.0	ν_{15},σ_u	2370
1808.1	ν_{16},σ_u	150
1650.0	ν_{17},σ_u	97755
1562.1	ν_{18},σ_u	2203
1290.8	ν_{19},σ_u	192
995.1	ν_{20},σ_u	8
679.4	ν_{21},σ_u	14
345.7	ν_{22},σ_u	45
1109.1	ν_{23},π_g	
750.0	ν_{24},π_g	
579.0	ν_{25},π_g	
491.2	ν_{26},π_g	
411.5	ν_{27},π_g	
282.2	ν_{28},π_g	
203.7	ν_{29},π_g	
129.9	ν_{30},π_g	
66.4	ν_{31},π_g	
21.2	ν_{32},π_g	
1102.3	ν_{33},π_u	10
737.1	ν_{34},π_u	1
565.9	ν_{35},π_u	4
505.0	ν_{36},π_u	0
453.0	ν_{37},π_u	0
313.0	ν_{38},π_u	0
239.4	ν_{39},π_u	2
165.7	ν_{40},π_u	4

Table 2-8. Continued

C_{23} calculated vibrational frequencies/cm^{-1} [b]	vibrational mode	intensity/km·mol^{-1}
96.3	ν_{41},π_u	4
41.0	ν_{42},π_u	3
7.7	ν_{43},π_u	2

[a] Bond lengths starting at terminal carbon
[b] Frequencies scaled by 0.95

frequency series (II) involves the same equal amplitude and out-of-phase motion in series I, but localized in each half of the molecule. Totally symmetric σ_g modes of the type discussed above should also be present in small chains. Although they have not yet all been observed, several have been extracted from IR combination bands[52] for n=5-7,9 and others have been calculated using DFT theory. These results are also shown in Figure 2-10 and Table 2-11. Calculated frequencies are used to fill in where experimental data are not yet available.

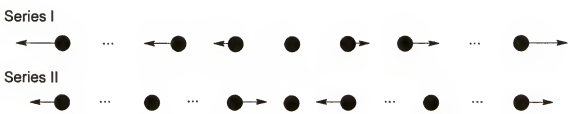

Figure 2-11. Relative motions of carbon atoms for Series I and Series II type vibrations observed in resonance Raman spectra.

C_{21} excitation profile. Plots of Raman band intensity, corrected for spectral response of the spectrometer and ν^4, against excitation wavelength are referred to as excitation profiles. Such a plot for a vibrational mode which is coupled to an electronic transition should essentially duplicate the absorption band profile. In Figure 2-9 the corrected intensities of the 192 cm^{-1} band are plotted against excitation wavelength. The superposition of the excitation profile and the 0-0 absorption band reveals a ~75 cm^{-1} blue shift of the excitation profile relative to the electronic absorption. This deviation

Table 2-9. Experimental resonance Raman frequencies and proposed assignments.

C_{15}		C_{17}		C_{19}		C_{21}		C_{23}	
observed bands[a]	assignment (calc freq)[b]	observed bands[a]	assignment (calc freq)[b]	observed bands[a]	assignment (calc freq)[b]	observed bands[a]	assignment (calc freq)[b]	observed bands[a]	assignment (calc freq)[b]
111		135		197		136		173	ν_{11},σ_g (174)
141	ν_{19},π_g (138)	220		214	ν_9,σ_g (210)	192	ν_{10},σ_g (190)	208	ν_{11}, ss[c]
219		237	ν_8,σ_g (235)	237	ν_9, ss[c]	217	ν_{10}, ss[c]	246	
267	ν_7,σ_g (266)	254	ν_8, ss[c]	266		268		270	
309		268		311		333		316	
367		342		371		381	$2\nu_{10}$	331	
437	ν_{17},π_g (424)	472	$2\nu_8$	425	$2\nu_9$	469		350	$2\nu_{11}$
533	$2\nu_7$	500		447		490		381	
659	ν_{15},π_g (678)	534		475		536	ν_{23},π_g (540)	474	
739		648		490		578	ν_9,σ_g (562)	494	
789	ν_6,σ_g (772)	698	ν_7,σ_g (687)	577		586		524	
919		738		627	ν_8,σ_g (619)	622		538	ν_{10},σ_g (515)
993		794	ν_{17},π_g (791)	649		655		564	
1035		868		732		731		596	
1056		962		781		773		656	
1137		990		853		839		766	
1209		1034		903	ν_{19},π_g (916)	891		804	
1259	ν_5,σ_g (1236)	1138		937		924	ν_8,σ_g (913)	959	
1324		1459		963		962		990	
1424		1600		987		997		1698	ν_6,σ_g (1697)
1457		1638		1045		1174		1758	
1511		1944		1589		1269		1850	
1639	ν_4,σ_g (1658)	1962		1823		1759		1960	ν_4,σ_g (1943)
1847		2037		1851		1822	ν_5,σ_g (1811)		
1921	ν_3,σ_g (1944)	2079		1869		1849			
1933		2112	ν_1,σ_g (2136)	1917	ν_4,σ_g (1909)				
1959				1951					
2035									

[a] Observed frequencies in cm^{-1}, [b] From B3LYP/6-311G* frequencies, in cm^{-1} scaled by 0.95, [c] Secondary trapping site

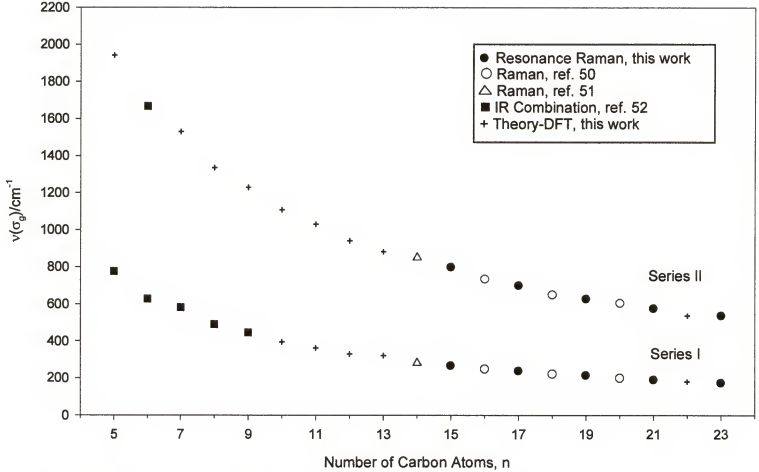

Figure 2-10. Plots of the two lowest totally symmetric σ_g vibrational frequencies for linear carbon clusters, C_n, as a function of n. Frequencies are from resonance Raman, Raman, IR combination bands, and DFT calculations ,B3LYP/6-311G* (C_{22}, C_{13}, C_{12}) and B3LYP/cc-pVDZ (C_5-C_{11}), where experimental values are not available.

Table 2-10. Vibrational frequencies of the two lowest energy totally symmetric, carbon-carbon stretching modes in linear carbon cluster isolated in Ar and N_2 matrices.

C_n	Raman Shift/cm^{-1} [a]	
n	Series I	Series II
23	173	538
22	181[b]	537[b]
21	192	578
20	200[c]	605[c]
19	214	627
18	223[c]	650[c]
17	237	698
16	249[c]	735[c]
15	267	798
14	282[d]	851[d]
13	323[b]	882[b]
12	331[b]	941[b]
11	363[b]	1031[b]
10	397[b]	1109[b]
9	445[e]	1229[b]
8	491[b]	1334[b]
7	582[e]	1529[b]
6	627[e]	1666[e]
5	775[e]	1943[b]

[a] Experimental, this work, unless otherwise noted.
[b] DFT, B3LYP/(6-311G*: C_{12},C_{13},C_{22}), (cc-pVDZ: C_5-C_{11})
[c] Ref. 47
[d] Ref. 49
[e] Ref. 52

is primarily due to the width of the 0-0 absorption,[73] i.e. the accuracy with which the excitation profile reproduces the absorption profile is limited by the width of the absorption profile. In this case the ~75 cm^{-1} shift is well within the ~200 cm^{-1} full width at half maximum of the C_{21} 0-0 band.

Summary

The following conclusions can be drawn from the present resonance Raman results. First, the assignment of the $^1\Sigma_u - {}^1\Sigma_g$ transitions of odd-numbered C_n clusters are consistent with the Raman results, and, by implication, so too should be the

electronic assignment of the clusters yet to studied with the Raman method. Second, the totally symmetric σ_g and π_g modes, predicted by density functional theory calculations, generally agree with experimental observations. Third, the Raman frequencies decrease with increasing chain length, and may be used as a diagnostic for specific chain lengths in the range studied here and perhaps beyond.

CHAPTER 3
CAVITY RINGDOWN SPECTROSCOPY

Introduction

Cavity Ringdown Spectroscopy, a technique originally developed to make precise measurements of laser mirror absorption losses,[74] has evolved into an ultra sensitive direct absorption technique capable of measuring concentrations on the order of 10^8 molecules/cm^3. Cavity Ringdown Spectroscopy (CRDS) in its present form is a multipass absorption technique developed by O'Keefe and Deacon in 1988,[75] and is simply the measurement of the rate at which light leaks out of an optical cavity. This method has several advantages over "conventional" absorption spectroscopies. The main advantage is that, for a given transition, CRDS offers higher sensitivity and lower detection limits than conventional absorption methods. CRDS differs from conventional absorption measurements in that it is based on the time rate of decay or ringdown time of a narrow band pulse of light injected into a stable optical cavity formed by two mirrors, as opposed to the conventional method of measuring the ratio of transmitted intensities. Since its inception CRDS has been applied from the UV to the IR regions.[76,77] It has also been demonstrated that a polychromatic light source can be used provided that the light exiting the cavity is spectrally analyzed using a Fourier transform spectrometer.[78] Additionally CRDS absorption spectra have also been measured using a cw probe laser.[79]

In the typical pulsed CRDS experiment a short (~10ns) laser pulse is injected into a stable optical cavity formed by two highly reflective ($R \geq 0.9999$) concave mirrors.

The fraction of light that enters the cavity reflects or "rings" back and forth many times, resulting in an effective path length for a 1m cavity of approximately 30km. With each trip a small portion, ~1-R, of light is transmitted through each mirror. The intensity of this transmitted light is monitored at the exit mirror with either a photomultiplier tube or a photodiode, resulting in a series of peaks whose intensities decrease exponentially (Figure 3-1). This decay profile is exponential due to the constant fraction of light lost upon each reflection. The rate can be described by equation 1. Here R is the reflectivity of the mirrors and t_r is the round trip time of the light pulse, and I is the light intensity.

$$\frac{dI}{dt} = -\left(\frac{1-R}{t_r/2}\right)I \tag{1}$$

Upon integration of this first order differential equation, a first order exponential solution is obtained:

$$I = I_o e^{-\left(\frac{1-R}{t_r/2}\right)t} \tag{2}$$

Additionally, since $t_r=2L/c$, where L is the length of the cavity and c is the speed of light, substitution into equation 2 allows for the characteristic ringdown time of the empty cavity, τ_o, to be determined:

$$\tau_o = \frac{L}{c(1-R)} \tag{3}$$

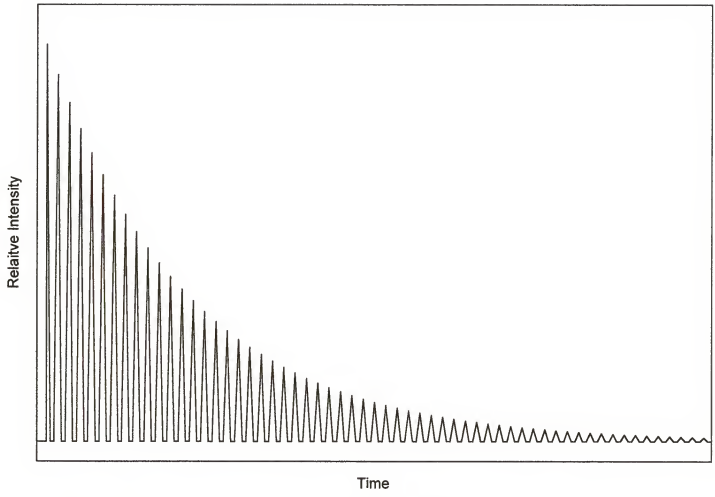

Figure 3-1. Typical ringdown signal, assuming the PMT is fast enough to detect each round trip.

This equation gives the per-pass optical loss of the cavity, which, if the cavity is evacuated, is due to the finite reflectivity of the mirrors. However, if an absorbing species is introduced into the cavity, such that the absorption follows Beer's Law for a single pass of the injected laser pulse, the absorption simply adds to the per-pass cavity loss. This results in a faster ringdown time. The solution to equation 1 then becomes:

$$I = I_o e^{-\left(\frac{(1-R)+A}{t_r/2}\right)t} \tag{4}$$

The per-pass absorption spectrum can be obtained by measuring τ as a function of wavelength of the injected light and solving equation 5.

$$A = \frac{t_r}{2}\left(\frac{1}{\tau} - \frac{1}{\tau_o}\right) \tag{5}$$

In practice, it is not necessary to measure τ_o independently, as over the course of the experiment it is relatively stable and changes primarily as a function of R. This allows for τ_o to be subtracted later by "eye" or fitting to a smooth function.

Two of the most important advantages of CRDS are its ability to measure transient events and the overall increase in sensitivity versus conventional absorption or multipass techniques. These two advantages were exploited in this study. Ultimately the goal is to use CRDS to measure the electronic absorption of PAH ions produced in a supersonic discharge, in order to determine their role as possible carriers of the DIBs.[13,35,81,82] However, the instrument first had to be tested for overall integrity, i.e. the ability to reproduce similar experiments described in the literature. For this test the

doubly forbidden b $^1\Sigma_g$ – X $^3\Sigma_g$ transition in O_2 will be measured. Next, the method of sample introduction must be explored. In these experiments the CRD absorption spectrum of a molecular beam of azulene, produced by a modified General Valve series 9 pulse valve, was probed. This tested nozzle design and, more importantly, allowed for the correct timing delay between the pulse valve and the firing of the probe laser to be determined. Finally, the electronic absorption of naphthalene cation was observed.

Cavity Ringdown Apparatus

Optical Cavity

The typical CRDS instrument consists of a stable optical cavity, a pulsed laser, a detector and a computer to control the instrument and process the data. Figure 3-2 shows a detailed block diagram of the instrument used in these experiments. Figure 3-3 is a representation of the actual cavity. The optical cavity is ~1m long and vacuum sealed by two highly reflective mirrors (R>99.99, 600-680nm) purchased from Research Electro-Optics, Inc. Keeping these mirrors clean was paramount and nitrogen or argon was flowed in front of the mirrors to form a protective curtain against deposits. In the pulsed discharge and supersonic expansion experiments the vacuum was maintained at $5x10^{-2}$ torr by a Leybold-Heraeus model WAU500/D90A roots pump system connected to the cavity by six-inch diameter PVC pipe. The pulse valve sources were connected to the cavity through an x,y,z translator. This translator also has an independent tilting motion allowing for rotation of the xy plane both parallel and perpendicular to the cavity axis.

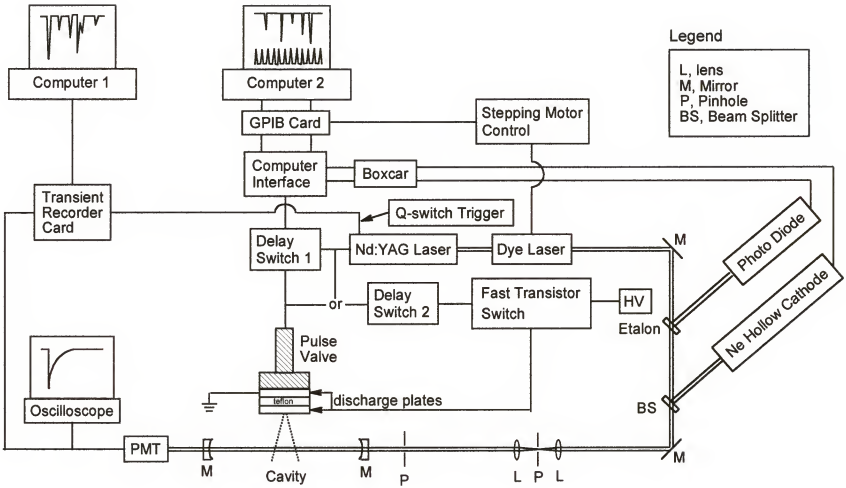

Figure 3-2. Block diagram of the Cavity Ringdown Spectroscopy Instrument

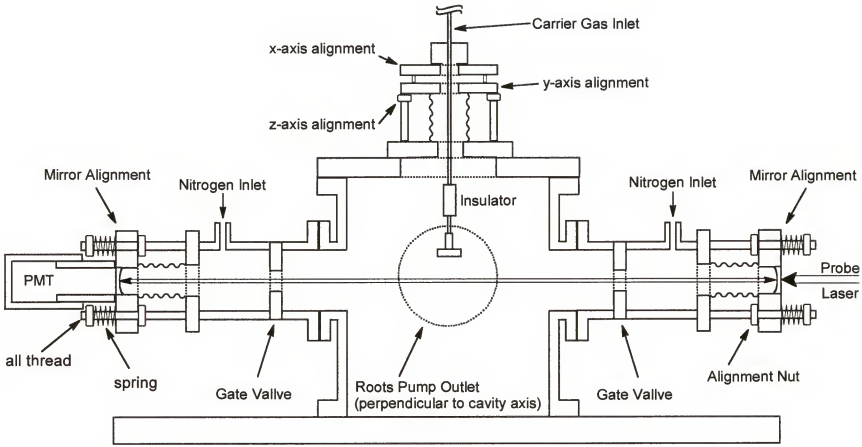

Figure 3-3. Cross section of CRDS instrument. Electrical feedthroughs, not shown, are located on the lid of the cavity, below the right arm and between the left arm and the roots pump connection. There is a three inch circular window mounted opposite the roots pump connection. The mirrors are mounted on alternating threaded and dowel rods placed around a six-fold axis. The mounts and alignment springs (placed around the threaded rod) are sandwiched by pairs of nuts. The mirror mounts and the x,y,z translator are connected to the vacuum chamber through bellows.

Laser System

A home made prism Littrow dye laser (Figure 3-4) pumped by a Spectra Physics model DCR-11 Nd:YAG laser was used as the probe laser. In all experiments the dye was $4x10^{-4}$ M DCM (4-Dicyanomethylene-2-methyl-6-p-diethylaminostyryl-4-H-pyran). This dye was chosen since it provides the best overlap of lasing action with respect to the high reflectivity range of the mirrors. The output of the dye laser was calibrated with a neon hollow cathode lamp utilizing the optogalvanic effect[82,83] (circuit shown in Figure 3-5).

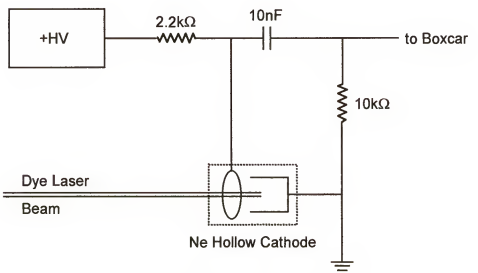

Figure 3-5. Optogalvanic Effect Circuit for dye laser calibration

Changes in lamp voltage were monitored when Ne electronic transitions are induced by the dye laser, Figure 3-6, upper trace. In the neon spectrum positive peaks corresponds to an initial decrease of ion current and negative peaks correspond to initial increase of ion current. From the shape of the neon peaks the bandwidth of the laser was determined to be ~$0.8cm^{-1}$. Additionally an etalon may be used in conjunction with the Ne hollow cathode. The spacing of the interference pattern produced by the etalon, Figure 3-6, lower trace, can be calculated using the equation $2nd \cos\theta = k\lambda$, where n is

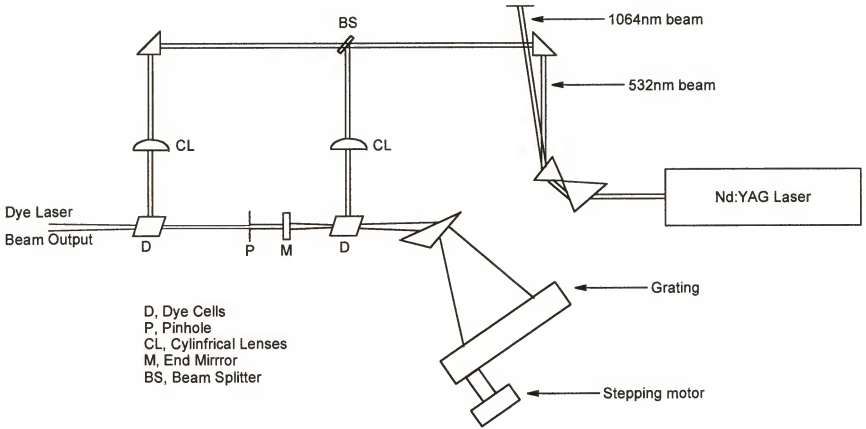

Figure 3-4. Multiple-prism Littrow Dye Laser

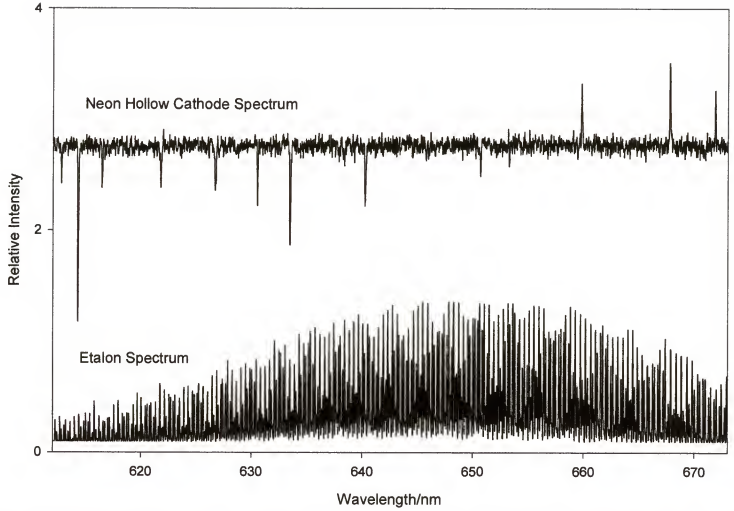

Figure 3-6. Neon hollow cathode spectrum (upper trace) and etalon spectrum (lower trace). These spectra cover the lasing range of the dye laser, ~610-675nm.

the index of refraction of the etalon material, d is the width of the etalon, θ is the angle of reflection normal to the incident beam with wavelength λ.[84] The signals from the hollow cathode lamp and the etalon, sampled via a photodiode, were averaged and stored on computer 1.

Triggering and Measurement of a Ringdown Transient

The measurement of a ringdown event is triggered by computer 1 which sends a 5V TTL pulse to delay switch 1 (Figure 3-7) which controls the delay between the triggering of the pulse valve and the Nd:YAG pump laser. As the Q-switch in the pump laser is initiated, a signal is sent to a transient recorder card in computer 2 which starts to record the output of the PMT. The PMT now begins to measure the ringdown signal from the cavity. Contrary to Figure 3-1, the detection of the decay in this system is slow compared to t_r ,and the decay appears to be continuous. Two examples of ringdown decay curves are shown in Figure 3-8. The ringdown time of the cavity, τ, is extracted by plotting the natural log of the decay curve and performing a linear least squares fit. The portion of the decay which is fit is variable, with the initial point being determined by the operator and the final point occurring when the initial intensity has decreased by an order of magnitude. Typically forty such ringdown events are averaged at a given wavelength before computer 1 steps the grating in the dye laser to a new wavelength and this process is repeated, generating τ as a function a function of wavelength. This spectrum is then stored on computer 2, and will be replotted as in equation 5.

Molecular Beam and Pulsed Discharge Sources

Several different molecular beam sources using different nozzle geometries were constructed and tested. Two geometries, a cylindrical beam source and a slit jet

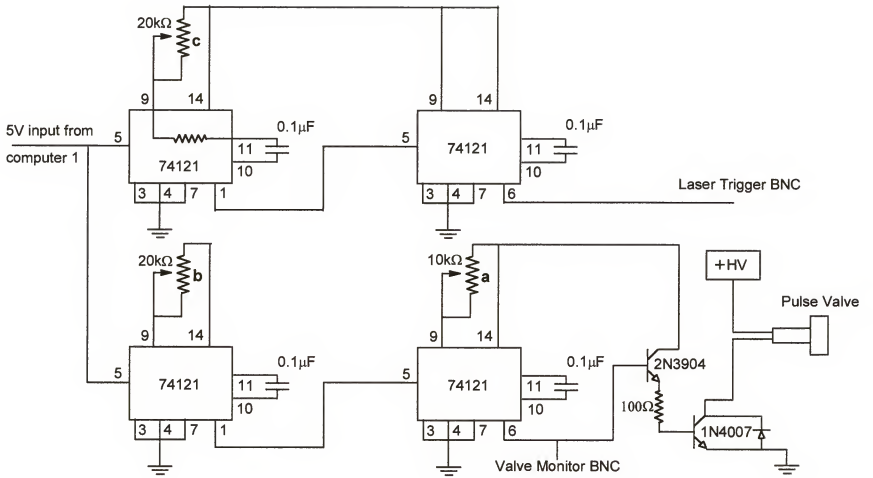

Figure 3-7. Schematic of control electronics for pulsed valve and laser firing, labeled delay switch 1. Potentiometers **a, b** and **c** control pulse valve width, pulse valve delay and laser delay, respectively.

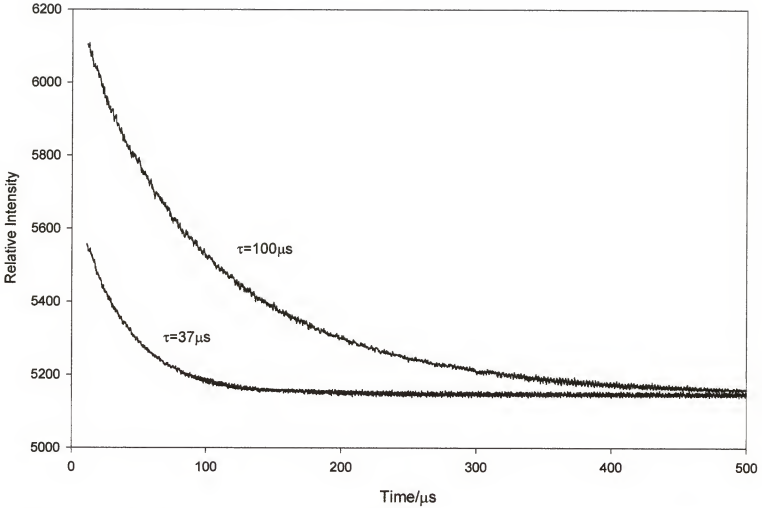

Figure 3-8. Observed intensity decay of a light pulse trapped inside the optical cavity. The upper trace represents a ringdown time of 100μs and the lower trace 37μs.

source, shown in Figure 3-9, produced stable discharges. With a suitable source for producing ions, attention was focused on how to vaporize the sample and mix it with the argon carrier gas. Initially, the heated sample container was placed in line with the carrier gas and approximately two inches above the pulse valve. This often resulted in condensation of the sample in the pulsed valve and/or in the throat of the nozzle. Condensation in the pulsed valve resulted in failure of the poppet seal. Condensation in the nozzle coated the electrodes resulting in an unstable discharge. This problem was solved by modifying a General Valve series 9 pulse valve as shown in Figure 3-10. These modifications were based on a pulsed source built by Li and Lubman.[85] The original valve solenoid and plunger were added to a custom-built pulsed valve flange with a two-piece stainless steel poppet. In order to vaporize the sample the source and the pulse valve are wrapped in heating tape. This assembly, with the use of Kalrez o-rings, may be heated to 185°C and has the advantage of having the sample directly in the pulse valve, precluding the need for a separate sample container. In addition, this is a more compact combination of the pulsed valve and sample container.

Experimental

CRD Absorption of Molecular Oxygen

To record the CRD spectrum of the b-X transition in O_2, the cavity was flooded with O_2, and the pressure maintained at ~1 atm. The dye laser was operated at a repetition rate of 10 Hz and pulse duration of 10 ns. The dye laser was stepped at 0.2 nm/data point from 625-635 nm. Forty ringdown transients were averaged at each data point.

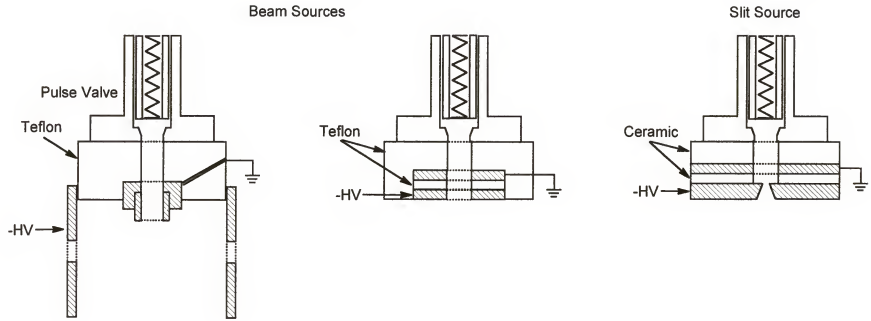

Figure 3-9. Cross section of several pulsed discharge sources. The left and middle sources represent molecular beam type sources and are cylindrical, The source on the right is a slit source and is square. In all three sources the high voltage electrode is stainless steel. In the left source the ground electrode is tantalum, and in the other two sources the ground electrode is stainless steel. In both beam sources the inside diameter of the throat is ~2mm, and, in the slit source, the slit formed by the ground electrode and the ceramic separator has dimensions 1.5x1.5x30mm. The aperture formed by the high voltage electrode is variable.

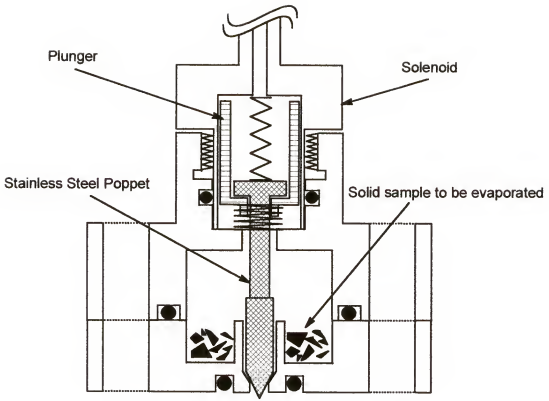

Figure 3-10. Modified Pulse Valve for solid samples. The valve solenoid and plunger are from a General Valve Series 9 pulse valve. The two piece flange body and poppet were custom-built. This design is based on a pulsed beam source described in Ref. 85.

CRD Absorption on Azulene

Experiments using the pulse valve for sample introduction required that the gas pulse was wide enough to overlap and coincide with the ringdown time. This was accomplished by delay switch 1. This switch was triggered by computer 1 and controled the delay between the firing of the pump laser and the opening of the pulse valve. It also regulated the pulse duration and operating voltage.

The $S_1(^1B_1)$-$S_0(^1A_1)$ transition in azulene was observed from 608-680 nm. The dye laser pulse was 10ns in duration with a repetition rate of 10Hz, and the grating was stepped at 0.5 Å increments. Forty ringdown events were averaged at each data point. The modified pulse valve was backed by 3 atm argon and was heated along with the

source to 75°C. The azulene-seeded jet intersected the probe laser 4-5 mm downstream of the nozzle. The gas pulse was ~1 ms in length and delayed 550 μs from the triggering of the Nd:YAG.

CRD Absorption of Naphthalene Cation

For pulsed discharge experiments an additional timing element was needed, delay switch 2 (Figure 3-11). This circuit triggers a fast transistor switch, dumping voltage to the discharge plates. This delay adjusts the triggering of the fast transistor switch relative to the opening of the pulse valve. It also controls how long the transistor switch stays open. This timing element was necessary to ensure the discharge was triggered when there was sufficient pressure of the carrier gas in the region of the discharge plates to produce an electrical discharge. This configuration, i.e. pulsing the discharge voltage, produces a more stable discharge than a continuous voltage on the discharge plates with the discharge initiated by the presence of the carrier gas.

The $D_2(^2B_{3g})$-$D_0(^2A_u)$ transition in $C_{10}H_8^+$ was observed using the same laser parameters as in the azulene experiments. The cavity was scanned from 640-675 nm, and eighty ringdown transients were averaged at each data point. The pulsed valve and source were heated to 115°C and the discharge plates were pulsed at 800 V.

Results and Discussion

The 2-0 Band of the Red Bands of Oxygen

To test the performance of the CRDS system the 2-0 band of the doubly forbidden $b\ ^1\Sigma_g - X\ ^3\Sigma_g$ transition of molecular oxygen was measured. This band system has been extensively studied by Babcock and Herzberg[86] and others.[87,88] Two factors contribute to the greatly reduced intensity of this system: it is a parity-forbidden and a

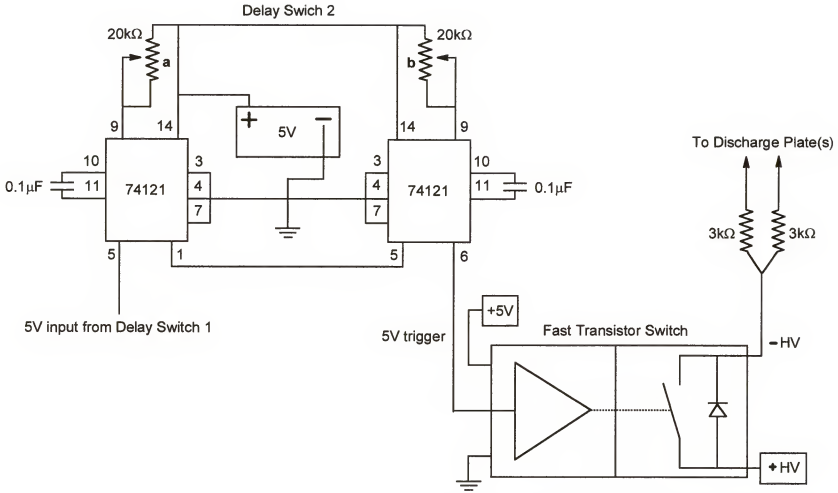

Figure 3-11. Delay Switch 2 and Fast Transistor Switch. Potentiometers **a** and **b** control the delay and width, respectively, of the 5V trigger sent to the Fast Transistor Switch.

spin-forbidden transition. Since the electric dipole transforms as u-type symmetry, a g-g transition is electric dipole forbidden and therefore must proceed through a magnetic dipole interaction. Also this transition is a singlet-triplet intercombination, violating the conservation of spin selection rule.

The $b\ ^1\Sigma_g - X\ ^3\Sigma_g$ absorption of molecular oxygen is shown in Figure 3-12. The ^RR and ^RQ components form the band head at 627.8 nm and the ^PP and ^PQ components stretch from 629 to 633.5 nm. The rotational transitions of these branches are diagrammed in Figure 3-13 and assignments tabulated in Table 3-1.

Table 3-1. Rotational assignments of 2-0 band of the $b\ ^1\Sigma_g - X\ ^3\Sigma_g$ absorption in O_2.

K"	^PP Branch/nm	^PQ Branch/nm
1	628.7	
3	629.0	628.9
5	629.3	629.2
7	629.6	629.5
9	269.9	629.8
11	630.3	630.2
13	630.6	630.5
15	631.0	630.9
17	631.4	631.4
19	631.9	631.8
21	632.4	632.3
23	632.9	632.8
25	633.5	633.4

Because this transition has been extensively studied and the measurements in this study agree with those in the literature, the other important information that can be extracted from this spectrum concerns detection limits and molar absorption coefficients. The intensity decay, measured by the PMT, may be described by equation 6.[89]

$$\frac{dI}{dt} = -I\left(\frac{\alpha c l}{nL} + \frac{1}{\tau_o}\right) \qquad (6)$$

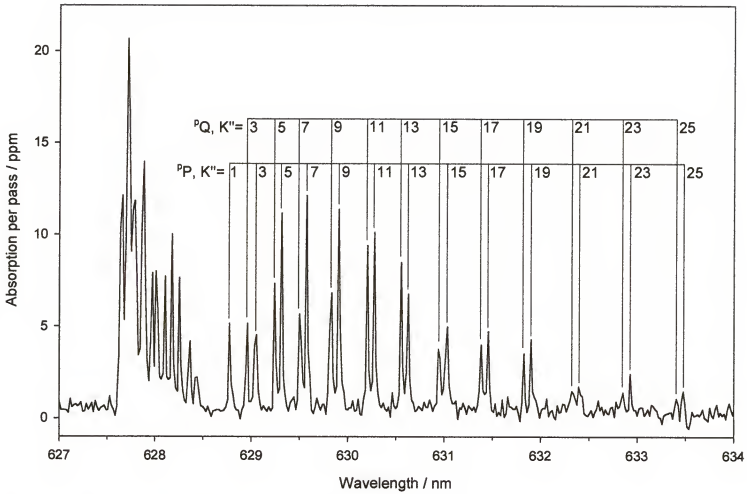

Figure 3-12. Absorption spectrum of the 2-0 band of the $b^1\Sigma_g$-$X^3\Sigma_g$ transition in molecular oxygen, recorded using a CRD spectrometer. Observed components of the ^{P}P and ^{P}Q branches are labeled. The ^{R}R and ^{R}Q branches, 627.5-628.5nm, cannot be assigned because of laser resolution.

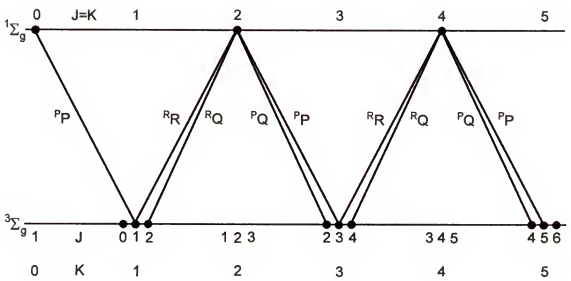

Figure 3-13. Potential energy diagram of the rotational level of the 2-0 band of the b-X absorption adapted from Babcock and Herzberg.[86] The solid lines represent rotational transitions, which obey the following selection rules: ^PP branch ($\Delta J = -1, \Delta K = -1$), ^RR branch ($\Delta J = 1, \Delta K = 1$), ^RQ branch ($\Delta J = 0, \Delta K = 1$), and a ^PQ branch ($\Delta J = 0, \Delta K = -1$).

where l is the number of photons injected into the cavity, $\alpha = \varepsilon[A]$; α is the absorption coefficient and ε is the molar absorption coefficient and [A] is the molar concentration of the absorbing species, c is the speed of light, l is the length of the absorbing medium, n is the index of refraction, L is the length of the cavity and τ_o is the characteristic ringdown time of the empty cavity. After integration, equation 6 becomes:

$$I = I_0 e^{-t/\tau_o} \tag{7}$$

where $1/\tau - 1/\tau_o = \alpha cl/nL$. Using the most intense component of the b-X bandhead at 627.8 nm, a molar absorption coefficient of 5×10^{-6} m^2/mol can be calculated from equation 7. Now if a typical molar absorption coefficient for an allowed transition is $\sim 10^4$ m^2/mol and assuming a conservative minimum detectable peak height of 4 μs, i.e. $\tau_o \sim \tau_{absorption}$, and τ_o=100 μs, the following detection limits may be extracted. For an allowed transition the

detection limit is $6x10^7$ molec/cm^3 and for a forbidden transition, with an ε value as above, the detection limit is $6x10^{17}$ molec/cm^3.

The S_1-S_0 Absorption of Azulene

Six months prior and unbeknownst to our group, researchers in Berlin published the CRD absorption of jet-cooled azulene.[90] Their objective was to obtain a well-resolved vibronic S_1 structure in order to extract the $S_{1,0}$ lifetime. Figure 3-14 shows the CRD spectrum of azulene from the slit source (cf. Figures 3-9,10), and Table 3-2 lists the observed band positions and assignments. The primary difference between this spectrum and that of Ruth *et al.*[90] is the appearance of low intensity red-shifted peaks accompanying the most intense spectral features. These red shifted bands are tentatively assigned to azulene- argon van der Waals complexes. This assignment is based on the relatively constant spacing between the unperturbed azulene modes and the corresponding argon-perturbed mode. The red-shifts and positions are summarized in Table 3-3.

However the purpose of this investigation was to test the modified pulse valve, find the best distance from the nozzle to the probe beam, and determine the optimal delay time between the firing of the probe laser and the opening of the pulsed valve, represented in Figure 3-15. There is an observed optimal delay, around 550 μs; however, the dependence of the CRD signal strength on delay time is not as critical as anticipated.

The D_2-D_0 Absorption of Naphthalene Cation

The CRD absorption spectrum of the $^2B_{3g}$-X^2A_u transition in $C_{10}H_8^+$ is shown in Figure 3-16. The CRD spectrum of $C_{10}H_8^+$ was previously measured by Romanini *et*

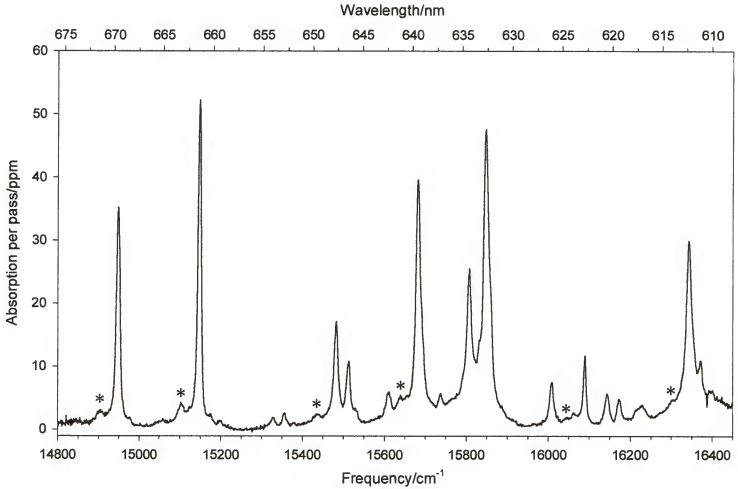

Figure 3-14. CRD spectrum of the S_1-S_0 tranistion of Azulene (this work) using the slit jet source with the following parameters: slit width=380μm, T=75°C, backing pressure=3atm Ar, laser delay=550μs. Bands marked with * are tentatively assigned to AzAr complexes.

Table 3-2. Band positions and assignments of the S_1-S_0 transition of jet-cooled Azulene.

ν^a/ cm^{-1}	$\Delta\nu^a$/ cm^{-1}	Relative Intensity[a]	$\Delta\nu^b$	$\Delta\nu^c$	$\Delta\nu_{obs}{}^a$-$\Delta\nu^b$	$\Delta\nu_{obs}{}^a$-$\Delta\nu^c$	Assignment	
							b	c
14284[c]							0_0^0	0_0^0
14903	619	3	615.3		4			
14948	664	66	661.3	664	3	0	16_0^1	16_0^1
14977	693	1						
15054	770	1	771.7	775	-2	-5	36_0^1	
15101	817	3						
15123	839	1						
15148	864	100	858.7	862	5	2	15_0^1	15_0^1
15174	890	1						
15198	914	1	910.8	913	3	1	14_0^1	14_0^1
			949.0					
15327	1043	3	1039.3	1041	4	2	35_0^1	$16_0^1\,17_0^1$
15355	1071	4	1068.0	1068	3	3	34_0^1	
15377	1093	1		1092				$15_0^1\,39_0^1$
15434	1150	2						
15481	1197	31	1194.8	1197	2	0	13_0^1	10_0^1
15511	1227	17	1223.9	1226	3	1	12_0^1	11_0^1
			1237.4				33_0^1	
15529	1245	1		1240		5		$15_0^1\,17_0^1$
15609	1325	6	1322.6	1324	2	1	16_0^2	16_0^2
			1344.2				32_0^1	
15638	1354	2						
15655	1371	1						
15682	1398	71	1394.1	1399	4	-1	10_0^1	9_0^1
15691	1407	shoulder	1405.6		1		31_0^1	
15737	1453	4	1449.5	1451	4	2	30_0^1	8_0^1
				1490				
				1504				
15807	1523	36	1520.0	1522	3	1	$15_0^1\,16_0^1$	$15_0^1\,16_0^1$
				1532				
15831	1547	shoulder	1545.0	1545	2	2	29_0^1	
15848	1564	90	1559.2	1566	5	-2	9_0^1	9_0^1
15860	1576	shoulder	1569.4		7		8_0^1	

Table 3-2. Continued

ν^a/ cm^{-1}	$\Delta\nu^a$/ cm^{-1}	Relative Intensity[a]	$\Delta\nu^b$	$\Delta\nu^c$	$\Delta\nu_{obs}{}^a$-$\Delta\nu^b$	$\Delta\nu_{obs}{}^a$-$\Delta\nu^c$	Assignment	
							b	c
								$17_0^1 11_0^1$
16008	1724	13	1717.5	1719	7	5	15_0^2	15_0^2
16043	1759	1						
16061	1777	1	1772.1	1771	5	6	$14_0^1 15_0^1$	$9_0^1 17_0^1$
16088	1804	20	1800.6	1801	3	3	7_0^1	
16142	1858	9	1853.2	1855	5	3	$13_0^1 16_0^1$	$16_0^1 10_0^1$
16172	1888	7	1883.2	1886	5	2	$12_0^1 16_0^1$	$16_0^1 11_0^1$
16216	1932	1	1925.8		6		$15_0^1 34_0^1$	
16229	1945	1	1941.2	1937	4	8		
16300	2016	2						
16343	2059	55	2052.7	2054	6	5	$13_0^1 15_0^1$	$15_0^1 10_0^1$
			2065.2				$16_0^1 31_0^1$	
16371	2087	6	2082.1	2083	5	4	$12_0^1 15_0^1$	$15_0^1 11_0^1$

[a] This Work, unless otherwise noted, [b] Ref. 90, [c] Ref. 91

Table 3-3. Azulene-Argon complex absorption band positions from the spectrum in Figure 3-14.

Azulene Argon Complexes			
Azulene Band Position/cm^{-1}	Complex Band Position/cm^{-1}	Intensity Ratio	Red Shift/cm^{-1}
664	619	26	45.0
863	817	31	47.0
1197	1150	20	47.0
1398	1354	34	44.0
1804	1759	16	45.0
2059	2016	32	43.0

al.[92] and is shown in Figure 3-17. These two experiments are identical except that in this work both the jet and the discharge are pulsed, whereas in the previous work the jet was continuous and the discharge was pulsed. The low signal-to-noise ratio seems to be inherent to the method for producing ions, due to a combination of background light from the discharge as well as low ion concentration. If there were an appreciable number of

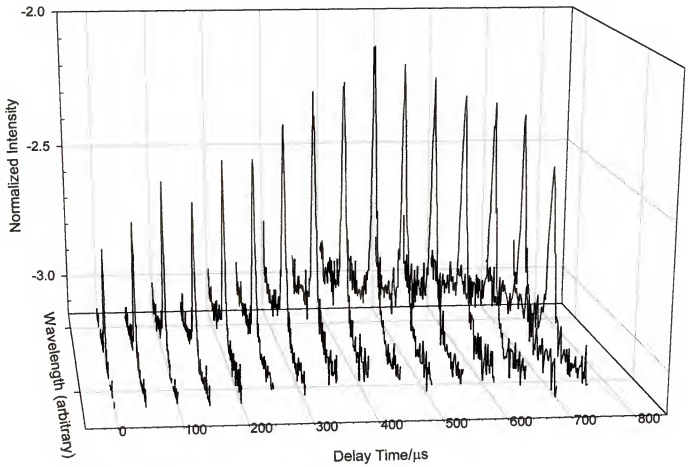

Figure 3-15. Profile of azulene 15147 cm^{-1} band as a function of delay time.

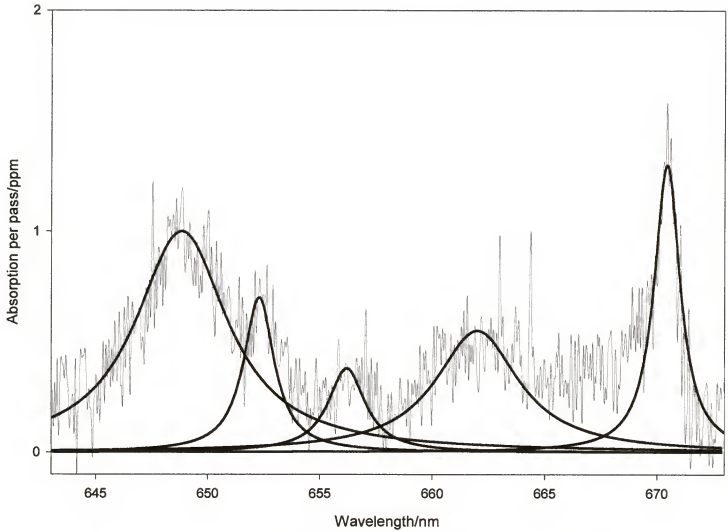

Figure 3-16. CRD spectrum of $^2B_{3g}$ (D_2) - X^2A_u (D_0) transition of $C_{10}H_8^+$ produced in a pulsed discharge (800V). Solid traces are Lorentzian fits of the ringdown signal.

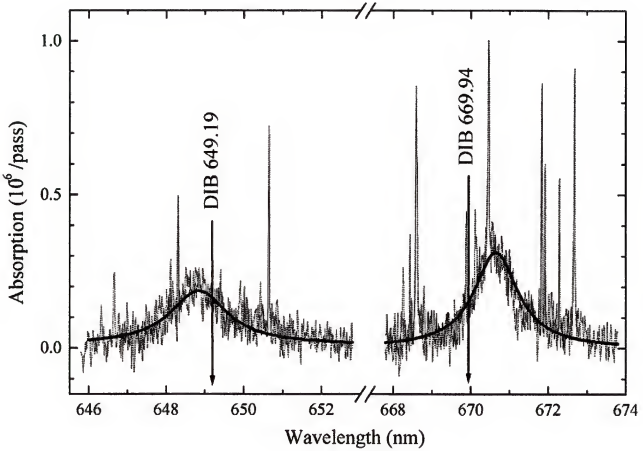

Figure 3-17. CRD spectrum taken from Romanini *et al.*[92] of bands at 670.65 and 648.84nm. The position of two DIBs are indicated.

$C_{10}H_8^+$ ions being produced, the CRD signal should be strong given that this transition is 10-100 times stronger that the S_1-S_0 transition in azulene. The observed bands in Figure 3-16 were fit to Lorentzian profiles and are centered at 648.8, 652.5, 656.5, 662.3, and 670.4 nm. The spacing and relative intensity of the 648.8 and 670.4 nm bands are in good agreement with previous matrix isolation experiments,[93] and the bands at 652.5, 656.5, and 662.3 nm are believed to be $C_{10}H_8^+$-Ar complexes. The positions of the 648.8 and 670.4 nm bands measured here agree with those of Romanini *et al.* and Pino *et al.*,[94] who measured the electronic absorption of $C_{10}H_8^+$ by a novel resonant two-photon two-color ionization. The width of the origin at 648.8 nm measured in this experiment is about two times the width of the same band measured by Romanini *et al.* This is most likely due to incomplete rotational cooling and is probably a result of the different jet configurations.

Comparing these two $C_{10}H_8^+$ bands with the weak DIBs at 646.19 and 669.94 nm[81] reveals a possible correspondence; however, it is unlikely that bands belonging to the same vibrational progression would display opposite shifts. Additionally, based on the more complete spectrum of Pino *et al.*, there is no correspondence between the DIBs and the $C_8H_{10}^+$ absorptions presented here.

Summary

A cavity ringdown absorption spectrometer was successfully built and demonstrated. The electronic absorption of a transient species, $C_{10}H_8^+$, was measured. The signal-to-noise ratio in this experiment was unusually low. This is due to background light from the argon discharge and low $C_{10}H_8^+$ concentration. To alleviate these problems, a more effective means of producing $C_{10}H_8^+$ in a jet must be used. However these experiments do demonstrate CRDS ability to measure the electronic spectra of gas-phase transient species.

CHAPTER 4
RED RECTANGLE BANDS AND C_3

Background

One of the most interesting problems in astrophysics today in the identity of the species responsible for the brilliant optical emission lines from the Red Rectangle Nebula. This unusual nebula is biconical in structure, is seen in both reflection and emission and surrounds the central star HD 44179. In addition to the so-called Red Rectangle Bands (RRBs), prominent optical emission bands which appear at 579.9, 585.3 and 591.3 nm, a broad extended red emission (ERE) is also observed from this source.

The RRB emission spectrum, Figure 4-1, was first observed in 1980 by Schmidt *et al.*[95] and has since been studied by several other research groups.[96-100] Since the relative intensities of the RRBs are invariant with respect to distance from the central star, it was concluded[97,98,101] that only one species gives rise to all the bands, that the species was a gas phase molecule and that the transitions originated from the same excited state vibrational level.

It has also been suggested that the emission in the Red Rectangle is linked to the diffuse interstellar bands (DIBs).[98,99,102,103] Sarre *et al.*[99] observed that several of the RRBs appear to arise from the same carriers of some of the DIBs. Figure 4-2 shows a comparison of the DIB spectrum (upper trace) and the RRB spectrum (lower trace) from 575 to 587 nm, demonstrating the correspondence between the DIBs and RRBs near 576.9, 580.0, and 585.3 nm.

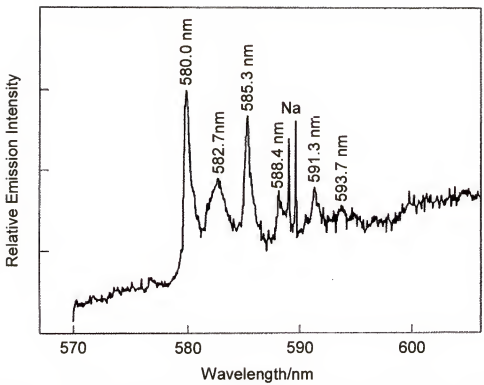

Figure 4-1. Emission spectrum of the nebula of the Red Rectangle from reference 96. It is suspected that emission from C_3 ($X^1\Sigma_g$-$a^3\Pi_u$) is responsible for this spectrum. The sodium D doublet is marked.

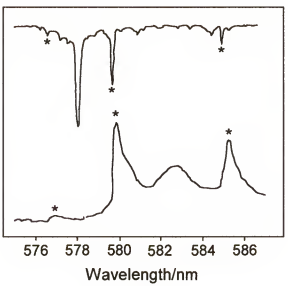

Figure 4-2. Comparison of the diffuse absorption band spectrum (upper trace) and the Red Rectangle spectrum (lower trace) adapted from reference 99. The stars mark correspondence between diffuse bands and Red Rectangle emissions near 576.9, 580.0, and 585.3 nm.

Phosphorescence from the carbon cluster, C_3, has been observed in rare gas matrices by several groups.[104-106] Figure 4-3 shows the spectrum of C_3 in an Ar matrix at 12 K observed previously in our lab. The resemblance to the RRBs is striking and has

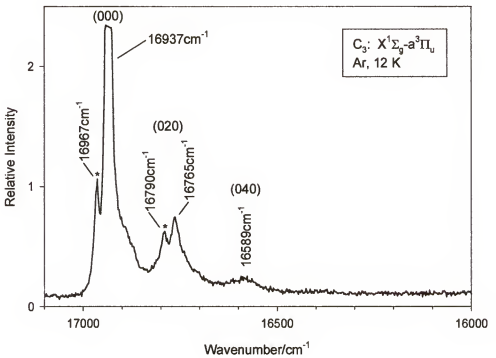

Figure 4-3. The phosphorescence spectrum of C_3 in Ar (12 K). The low intensity blue shifted peak denoted by * are secondary trapping sites. Origins and vibrational assignments are noted. Vibrational assignments are labeled by the number of quanta in ($\nu_1\nu_2\nu_3$) modes.

led other groups to suggest gas phase C_3 as the carrier of the RRB spectrum.[95,96,101] In particular Glinski and Nuth propose a specific C_3 vibrational assignment for the observed RRB system. One controversial aspect of this assignment, however, is the suggestion that the origin band is not observed. The authors claim the reason for this is the expected small spin-orbit coupling (SOC) with allowed singlet-singlet transitions. They

state that "... direct comparison of the matrix spectrum with a gas phase spectrum may not be appropriate." Their contention of minimal SOC in such a small molecule is suspect, however, since phosphorescence (and therefore SOC) is observed in formaldehyde, H_2CO, a molecule with even fewer electrons.[107] The authors' suggestion of an experiment to determine the gas-phase phosphorescence of C_3 is an excellent one. We suggest two methods later to accomplish this goal.

One interesting aspect of the C_3 phosphorescence observed in matrices is the presence of bands only in even quanta of the bending mode. Odd quanta are forbidden due to the ungerade character of this mode. However, if C_3 were somehow made unsymmetrical, as in a complex, the odd modes would become allowed. In that case, the spectrum might more closely resemble the RRB emission.

Carbon clusters are known to form complexes with water.[108,109] Infrared and electronic absorption spectra of the $C_3 \cdot H_2O$ complex have been studied previously in this lab.[108] But the emission spectrum of $C_3 \cdot H_2O$ has not yet been observed. To do this experiment, the $C_3 \cdot H_2O$ complex was produced by laser ablation of graphite in the presence of 3% H_2O/Ar mixture and deposited on a silver coated copper cold finger. This complex is known to absorb at 405 nm.[108] This wavelength was selected using a Xe lamp (1000 W) and a 0.25 m excitation monochromator. Emission from the matrix was collected and analyzed with a double monochromator (1 m) using photon counting detection. The upper spectrum in Figure 4-6 reveals a vibrational progression of $C_3 \cdot H_2O$ that has an average spacing of ~105 cm^{-1} and is blue shifted from C_3 by ~400 cm^{-1}. Complexes of carbon clusters with water are usually destroyed upon uv irradiation. The lower trace in figure 4-6 is after one hour photolysis with a medium pressure Hg lamp. Only emission from C_3 is now observed which confirms that the photo-bleached bands belong to $C_3 \cdot H_2O$. Previous experiments on the photochemistry of $C_3 \cdot H_2O$[108] have shown that photolysis of the complex results in the formation of C_3O and

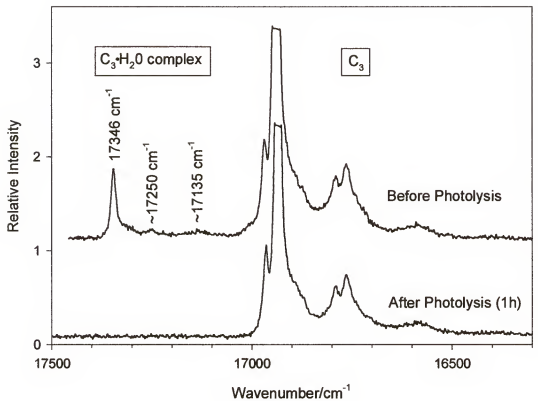

Figure 4-6. Emission spectra of C_3•H_2O and C_3 in Ar (12 K) before (upper trace) and after photolysis (lower trace) with a medium pressure Hg lamp. Emission from the C_3•H_2O complex is labeled. No additional emission was observed after photolysis.

3-hydroxypropadienylidene. In the present experiments no additional emission was observed after matrix photolysis. Based on the energy and spacing of the emission and the photolysis behavior, C_3•H_2O does not appear to be the carrier of the RRBs.

Future Experiments to Measure Gas-Phase C_3 Phosphorescence

In the first method, C_3 would be produced by laser ablation of graphite in the presence of Ar. The $A^1\Pi_u$-$X^1\Sigma_g$ transition would be excited by the ablation plasma, and

detection of emission would be accomplished using a pulsed ICCD (Intensified CCD) camera and monochromator. In the second method, C_3 would be produced in a molecular beam either by laser ablation of graphite or by a pulsed electrical discharge of C_2H_2. The $A^1\Pi_u$-$X^1\Sigma_g$ transition would be pumped using a cw frequency-doubled Ti:sapphire laser or a pulsed dye laser, and any emission would be detected using a monochromator and detector.

A diagram of the apparatus proposed to measure C_3 phosphorescence by the first method is shown in Figure 4-4. C_3 clusters are produced by oscillating a slightly

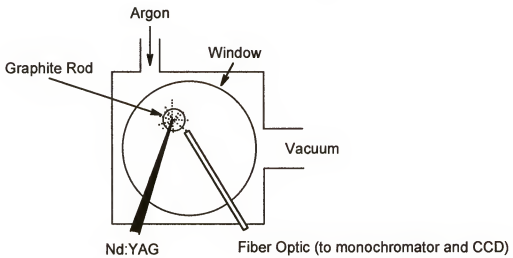

Figure 4-4. Diagram of laser ablation configuration proposed to measure C_3 phosphorescence. C_3 molecules are excited during vaporization by the Nd:YAG laser. Emission is collected by the fiber optic and analyzed with a monochromator and pulsed CCD.

focused Q-switched Nd:YAG laser (1064/532 nm, 10 Hz, 10-20 mJ) across the end of a graphite rod. The $A^1\Pi_u$-$X^1\Sigma_g$ transition would be effected by the resulting ablation plasma. The C_3 cluster would undergo intersystem crossing to the $a^3\Pi_u$ excited state and then radiatively relax to the $X^1\Sigma_g$ ground state. Phosphorescence would be observed by operating the CCD camera in pulsed mode, i.e. the timing of the camera

would be such that light from the Nd:YAG laser, and possibly the plasma, would be rejected and emission by molecules in the plasma detected.

In the second experiment, C_3 clustesr would be produced in a molecular beam by either of the two sources. One method would be to use a pulsed electrical discharge of 1% C_2H_2/Ar using any of the three discharge sources described earlier (cf. Figure 3-9).

Another possible cluster source is a Smalley source.[110] This device, Figure 4-5, was developed in R. E. Smalley's research group during the early 1980s. In this cluster source, the carrier gas passes over a rotating rod (in this case a graphite rod) as the laser vaporizes the surface of the rod. Ablation products are carried downstream and flow into the vacuum chamber. After formation of the clusters, a cw frequency-doubled Ti:sapphire laser (408 nm, 10 mW) or pulsed N_2-pumped Stilbene 420 dye laser would be aligned coaxially with the molecular beam to excite the $A^1\Pi_u$-$X^1\Sigma_g$ transition. Any emission from the molecular beam would be collected, 90° relative to the beam axis, and focused into a monochromator. Figure 4-6 is a diagram of the molecular beam apparatus proposed to measure gas phase C_3 phosphorescence.

Either of the two experiments proposed here would allow for the gas phase observation of the spin forbidden $X^1\Sigma_g$-$a^3\Pi_u$ transition in C_3, and hopefully solve the puzzle concerning C_3 and the Red Rectangle Bands.

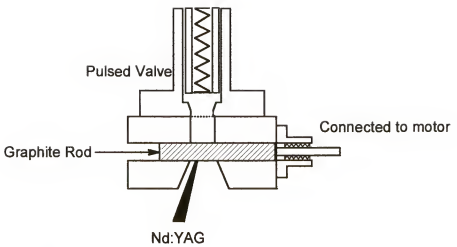

Figure 4-5. Smalley cluster source. Clusters are produced by laser ablation of a rotating target rod. The timing of the laser pulse with respect to the opening of the pulse valve is such that there is a maximum pressure of the carrier gas at the vaporization point.

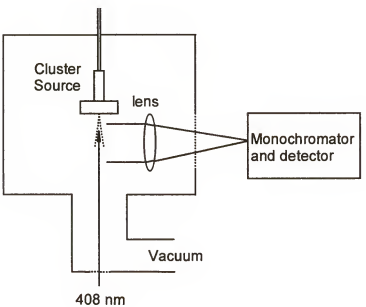

Figure 4-5. Diagram of molecular beam configuration proposed to measure gas phase C_3 phosphorescence. C_3 clusters are produced in molecular beam and excited with frequency doubled Ti:sapphire laser. Emission is collected with a lens and focused in a monochromator.

CHAPTER 5
SUMMARY

The research presented in this dissertation encompasses two projects. The ultimate goal of these projects is to gain a better understanding the role of carbon-bearing species in the interstellar medium. The first project was matrix isolation resonance Raman spectroscopy of linear carbon clusters, and the second project was the construction and development of a cavity ringdown spectroscopy instrument for measuring absorption of transient species, specifically PAH ions.

Resonance Raman Spectroscopy. The following conclusions can be drawn from the present resonance Raman results. First, the assignment of the $^1\Sigma_u$-$^1\Sigma_g$ transitions of odd numbered C_n clusters are consistent with the Raman results, and, by implication, so too should be the electronic assignment of the clusters yet to studied with the Raman method. Second, the totally symmetric σ_g and π_g modes, predicted by density functional theory calculations, generally agree with experimental observations. Third, the Raman frequencies decrease with increasing chain length, and may be used as a diagnostic for specific chain lengths in the range studied here and perhaps beyond.

Cavity Ringdown Spectroscopy. A cavity ringdown absorption spectrometer was successfully built and demonstrated. The doubly forbidden ($^1\Sigma_u$-$^3\Sigma_g$) transition in molecular oxygen was measured to test the integrity of the instrument and determine the instrument's detection limits. The S_1-S_0 transition of gas phase azulene was measured to test the method of sample introduction and determine the correct timing delays between the opening of the pulse valve and firing the probe laser. Finally, the electronic absorption of a transient species, $C_{10}H_8^+$, was measured. These experiments do

demonstrate the ability of CRDS to measure the electronic spectrum of gas-phase transient species.

APPENDIX
PARTICLE-IN-A-BOX FORMALISM APPLIED TO CARBON CHAINS

This analysis describes the linear relation between the number of carbon atoms in an odd-numbered, neutral chain and the wavelength of the 0-0 electronic transition with in the particle-in-a-box (PIB) framework. The energy of a PIB system is

$$E_N = \frac{N^2 h^2}{8mL^2} \quad (1)$$

In this equation, N designates a specific energy level, h is Planck's constant, m is the mass of the particle, and L is the length of the box. When applied to carbon clusters L and N may be defined as a function of the number of carbon atoms (n) in the C_n cluster. First let the L=(n-1)l + l, where n is the number of carbon atoms in the C_n cluster and l is the average length of a C-C bond. Additionally 1/2 l is added to each end of the chain to better model the confinement of the electrons, resulting in L=nl. Concerning N, for a carbon chain with n atoms there 4n valence electrons: 2n-2 electrons are in n-1 σ orbitals, four electrons are in terminal orbitals, and the remaining 2n-2 electrons populate the π system. Since the π orbital is doubly degenerate it can accommodate 4 electrons, and odd-numbered chains will fill the lowest (n-1)/2 π orbitals resulting in a $^1\Sigma_g$ ground state.[111] From this description, the HOMO in an odd-numbered linear carbon cluster (C_n) is the (n-1)/2 π orbital. Now considering a HOMO-LUMO transition, it can be seen that for an odd-numbered cluster, N_{HOMO}=(n-1)/2 and N_{LUMO}=(n+1)/2. Substituting N and L expression into equation 1 for a HOMO-LUMO transition, ΔE is

$$\Delta E = \frac{h^2}{8m(nl)^2}\left[\frac{(n+1)^2}{4} - \frac{(n-1)^2}{4}\right] \quad (2)$$

After rearrangement,

$$\Delta E = \frac{h^2}{8mnl^2} \quad (3)$$

and since $\Delta E = hc/\lambda$, (c is the speed of light and λ is wavelength) equation 3 may be rearranged to show the linear relation between λ and n.

$$\lambda = \frac{8mcl^2}{h} n \quad (4)$$

Now it is seen that a graph of λ vs n is linear with slope $8mcl^2/h$. If the slope of this line is measured from Figure 2-2 for carbon clusters C_{25}-C_{13} an average bond length of 0.84 Å is extracted. This bond length, compared to calculated values of ~1.28 Å, is 35 % too small. However, if the 0-0 electronic transition is assumed to be from the (n-2)/2 bonding π orbital to the (n+2)/2 antibonding π orbital and applying the same method described above, a bond length of 1.18 Å is extracted which is only 8% too small.

REFERENCES

1. P. Ehrenfreund and S. B. Charnley, *Annu. Rev. Astron. Astrophys.*, **2000**, *38*, 427.

2. G. Knapp, *Sky and Telescope*, **1995**, *May*, 23.

3. M. Spaans, and P. Ehrenfreund, In *Laboratory Astrophysics and Space Research*, ed. P Ehrenfreund, K. Krafft, H. Kochan, and V. Pirronello, Dordrecht: Kluwer, **1999**.

4. R. Campargue, ed., *Atomic and Molecular Beams: The State of the Art 2000*, Springer-Verlag: Berlin, **2001**.

5. M. J. Travers, M. C. McCarthy, P. Kalmus, C. A. Gottlieb, and P. Thaddeus, *Astrophys. J.*, **1996**, *469*, L65.

6. M. B. Bell, P. A. Feldman, M. J. Travers, M. C. McCarthy, C. A. Gottlieb, and P. Thaddeus, *Astrophys. J.*, **1997**, *483*, L61.

7. D. J. Hollenbach and A. G. G. M. Tielens, *Annu. Rev. Astron. Astrophys.*, **1997**, *35*, 179.

8. E. F. van Dishoeck, In *The Molecular Astrophysics of Stars and Galaxies*, ed. T. W. Harquist and D. A. Williams, Oxford University Press: Oxford, **1998**.

9. T. J. Millar, E. Herbst, and R. P. A. Bettens, *Mon. Not. R. Astron. Soc.*, **2000**, *316*, 195.

10. P. W. Merrill, *Publ. Astron. Soc. Pacific*, **1934**, *46*, 206.

11. P. W. Merrill, *Astrophys. J.*, **1936**, *83*, 126.

12. G. H. Herbig, *Astrophys. J.*, **1988**, *331*, 999.

13. G. H. Herbig, *Annu. Rev. Astron. Astrophys* **1995**, *33*,19.

14. S. O'Tuairisg, J. Cami, B. H. Foing, P. Sonnentrucker, and P. Ehrenfreund, *Astron. Astrophys. Suppl.*, **2000**, *142*, 225.

15. P. Ehrenfreund, J. Cami, E. Dartois, and B. H. Foing, *Astron.* Astrophys., **1997**, *318*, L28.

16. F. Salama, E. L. O. Bakes, L. J. Allamandola, and A. G. G. M. Tielens, *Astrophys. J.*, **1996**, *458*, 621.

17. P. Bréchignac and T. Pino, *Astron. Astrophys.*, **1999**, *343*, L49.

18. P. Freivogel, J. Fulara, and J. P. Maier, *Astrophys. J.*, **1994**, *431*, L151.

19. M. Tulej, D. A. Kirkwood, M. Pachkov, and J. P. Maier, *Astrophys. J.*, **1998**, *506*, L49.

20. P. Ehrenfreund, and B. H. Foing, *Astron. Astrophys.*, **1996**, *307*, L25.

21. B. H. Foing and P. Ehrenfreund, *Astron. Astrophys.*, **1997**, *317*, L59.

22. J. K. G. Watson, *Astrophys. J.*, **1994**, *437*, 678.

23. L. J. Allamandola, D. M. Hudgins, W. Bauschlicher, and S. R. Langhoff, *Astron. Astrophys.*, **1999**, *352*, 659.

24. T. Motylewski, H Linnartz, O. Vaizert, J. P. Maier, and G. A. Galazutdinov, *Astrophys. J.*, **2000**, *531*, 312.

25. F. C. Gillet, W. J. Forrest, and K. M. Merrill, *Astrophys. J.*, **1973**, *183*, 87.

26. R. Russel, B. Soifer, S. Willner, *Astrophys. J.*, **1977**, *217*, L149; **1978**, *220*, 568.

27. A. G. G. M. Tielens, S. Hony, C. van Kerckhoven, and E. Peeters, In *The Universe as seen by ISO*, *427*, 579, ESA Publishing Division: Noordwijk, **1999**.

28. A. Leger, and J. L. Puget, *Astron. Astrophys.*, **1984**, *137*, L5.

29. L. J. Allamandola, A. G. G. M. Tielens, and J. R. Barker, *Astrophys. J.*, **1985**, *290*, L25.

30. J. Szczepanski, and M. Vala, *Nature*, **1993**, *363*, 699.

31. C. Joblin, A. G. G. M. Tielens, T. R. Geballe, D. H. Wooden, *Astrophys. J.*, **1996**, *460*, L119.

32. G. C. Sloan, T. L. Hayward, L. J. Allamandola, J. D. Bregman, B. DeVito, and D. M. Hudgins, *Astrophys. J.*, **1999**, *513*, L65.

33. E. Whittle, D. A. Dows, and G. C. Pimental, *J. Chem. Phys.*, **1954**, *22*, 1943.

34. S. Cradock and A. J. Hinchcliffe, *Matrix Isolation: A technique for the study of reactive inorganic species*, Cambridge University Press: Cambridge, **1975**.

35. L. Andrews and M Moskovits, *Chemistry and Physics of Matrix-Isolated Species*, North-Holland: Amsterdam, **1989**.

36. N. F. Ramsey, *Molecular Beams*, Oxford University Press: Oxford, **1956**.

37. J. M. Hollas and D. Phillips, eds., *Jet Spectroscopy and Molecular Dynamics*, Blackie Academic and Professional: Glasgow, **1995**.

38. W. R Gentry and C. F. Giese, *Rev. Sci. Instrum.*, **1978**, *49*, 595.

39. R. L. Beyer and M. D. Duncan, *J. Chem. Phys.*, **1981**, *74*, 2174.

40. F. M. Behlen, N. Mikami and S. A. Rice, *Chem. Phys. Lett.*, **1979**, *60*, 354.

41. J. B. Hopkins, P. R. R. Langridge-Smith, M. D. Morse, and R. E. Smalley, *J. Chem. Phys.*, **1983**, *78*, 1627.

42. W. Weltner and R. J. Van Zee, *Chem. Rev.* **1989**, *89*, 1714.

43. A. Van Orden and R. J. Saykally, *Chem. Rev.* **1998**, *98*, 2313.

44. J. Szczepanski, S. Eckern, and M. Vala, *J. Phys. Chem.*, **1997**, *101*, 1841.

45. J. Szczepanski, S. Eckern, Chris Chapo, and M. Vala, *Chem. Phys.*, **1996**, *211*, 359.

46. A. Van Orden, R. A. Provencal, F. N. Keutsch, and R. J. Saykally, *J. Chem. Phys.*, **1996**, *105*, 6111.

47. T. L. Haslett, S. Fedrigo, and M. J. Moskovits, *J. Chem. Phys.* **1997**, *103*, 7815.

48. D. W. Arnold, S. E. Bradforth, T. N Kitsopoulos, and, D. M. Neumark, *J. Chem. Phys.* **1991**, *95*, 8753.

49. C. Xu G. R. Burton, T. R. Taylor, and D. M. Neumark, *J. Chem. Phys.* **1997**, *107*, 3428.

50. A. K. Ott, G. A. Rechtsteiner, F. Christian, O. Hampe, M. F. Jarrold, R. P. Van Duyne, and K. Raghavachari, *J. Chem. Phys.* **1998**, *109*, 9652.

51. G. A. Rechtsteiner, F. Christian, A. K. Ott, O. Hampe, R. P. Van Duyne, M. F. Jarrold, and K. Raghavachari, *J. Phys. Chem.* **2001**, *105*, 3029.

52. J. F. Fuller, J. Szczepanski, and M. Vala, *Chem. Phys. Lett.* **2000**, *323*, 86.

53. T. Onaka, I. Yamamura, T. Tanabe, T. L. Roellig, and L. Yuen, *Publ. Astron. Soc. Japan* **1996**, *48*, L59.

54. A. E. Douglas, *Nature* , **1977**, *269*, 130.

55. A. Leger and L. d'Hendecourt, *Astron. Astrophys.*, **1985**, *146*, 81.

56. J. P. Maier, *J. Phys. Chem.*, **1998**, *102*, 3462 and references therein.

57. G. A. Galazutdinov, J. Krelowski, and F. A. Musaev, *Mon. Not. R. Astron. Soc.*, **1999**, *310*, 1017.

58. B. J. McCall, D. G. York, and T. Oka, *Astrophys. J.*, **2000**, *531*, 329.

59. D. P. Ruffle, R. P .A. Bettens, T. Terzieva, and E. Herbst, *Astrophys. J.*, **1999**, *523*, 678.

60. W. Weltner, Jr. and D. McLeod, Jr., *J. Chem. Phys.*, **1966**, *45*, 3096.

61. W. Kratschmer, N. Sorg, and D. Huffman, *Surface Sci.*, 1985, *156*, 814; W. Kratschmer, K.Nachtigal, in: A. Leger, L. d'Hendecourt (Eds.), *Polycyclic Aromatic Hydrocarbons and Astrophysics*, NATO-ASI Series: Reidel, Dordrecht, 1987.

62. P. Freivogel, J. Fulara, M. Jacobi, D. Forney, and J. P. Maier, *J. Chem. Phys.*, **1995**, 103, 54.

63. D. Forney, P. Freivogel, M. Grutter, and J. P. Maier, *J. Chem. Phys.*, **1996**, *104*, 4954.

64. M. Wyss, M. Grutter and J. P. Maier, *Chem. Phys. Letters*, **1999**, *304*, 35.

65. J. Szczepanski, J. Fuller, S. Eckern, and M. Vala, *Spectrochimica Acta A*, **2001**, *57*, 775.

66. K. W. Chang and W. R. M. Graham, *J. Chem. Phys.*, **1982**, *77*, 4300.

67. J. Kurtz and D. Huffman, *J. Chem. Phys.*, **1990**, *92*, 30.

68. J. Szczepanski and M. Vala. *J. Phys. Chem.*, **1991**, *95*, 2792.

69. Gaussian 98, Revision A.6, M. J. Frisch, G. W. Trucks, H. B. Schlegel, G. E. Scuseria,M. A. Robb, J. R. Cheeseman, V. G. Zakrzewski, J. A. Montgomery, Jr., R. E. Stratmann, J. C. Burant, S. Dapprich, J. M. Millam, A. D. Daniels, K. N. Kudin, M. C. Strain, O. Farkas, J. Tomasi, V. Barone, M. Cossi, R. Cammi, B. Mennucci, C. Pomelli, C. Adamo, S. Clifford, J. Ochterski, G. A. Petersson, P. Y. Ayala, Q. Cui,K. Morokuma, D. K. Malick, A. D. Rabuck, K. Raghavachari, J. B. Foresman, J. Cioslowski, J. V. Ortiz, B. B. Stefanov, G. Liu, A. Liashenko, P. Piskorz, I. Komaromi, R. Gomperts, R. L. Martin, D. J. Fox, T. Keith, M. A. Al-Laham, C. Y. Peng, A. Nanayakkara, C. Gonzalez, M. Challacombe, P. M. W. Gill, B. Johnson, W. Chen,M. W. Wong, J. L. Andres, C. Gonzalez, M. Head-Gordon, E. S. Replogle, and J. A. Pople, Gaussian, Inc., Pittsburgh PA, 1998.

70. A. D. Becke, *J. Chem. Phys.*, **1993**, *98*, 5648.

71. F. A. Cotton, *Chemical Applications of Group Theory, 3rd ed.,* Wiley-Interscience: New York, **1990**.

72. D. M. Bishop, *Group Theory and Chemistry*, Dover Publications, Inc.: New York, **1973**.

73. R. J. H. Clark, In *NATO Advanced Study Institute on Vibronic Processes in Inorganic Chemistry*, ed. C. D. Flint, Kluwer Academic Publishers: Boston,**1989**.

74. J.M. Herbelin, J.A. McKay. M.A. Kwok, R.H. Ueunten, D. S. Urevig, D. J. Spencer, and D. J. Benard, *Appl. Opt.* **1980**, *19*, 144.

75. A. O'Keefe and D. A. G. Deacon, *Rev. Sci. Instrum.* **1988**, *59*, 2544.

76. J. J. Scherer, D. Voekel, D. J. Rakestraw, J. B. Paul, C. P. Collier, R. J. Saykally, and A. O'Keefe, *Chem. Phys. Lett.* **1995**, *245*, 273.

77. J. J. Scherer, J. B. Paul, A. O'Keefe, and R. J. Saykally, *Chem. Rev.* **1997**, *97*, 25.

78. R. Engeln, and G. Meijer, *Rev. Sci. Instrum.* **1996**, *67*, 2708.

79. D. Romanini, A. A. Kachanov, and F. Stoeckel, *Chem. Phys. Lett.*, **1997**, *270*, 546.

80. P. Jenniskens and F. X. Désert, *Astron. Astrophys. Suppl. Ser.* **1994**, *106*, 39.

81. G. P. Van der Zwet and L. J. Allamandola, *Astron. Astrophys.* **1985**, *146*, 76.

82. R. B. Green, R. A. Keller, G. G. Luther, P. K. Schenck, and J. C. Travis, *Appl. Phys. Lett.* **1976**, *29*, 727.

83. D. S. King, P. K. Schenck, K. C. Smyth, and J. C. Travis, *Appl. Optics.* **1977**, *16*, 2617.

84. G. R. Fowles, *Introduction to Modern Optics, 2nd Ed.*, Dover Publication, Inc.: New York, **1975.**

85. L. Li and D. M. Lubman, *Rev. Sci. Instrum.* **1989**, *6*, 499.

86. H. D. Babcock and L. Herzberg, *Astrophys. J.* **1948**, *108*, 167.

87. W. F. Giauque and H. L. Johnson, *J. Am. Chem. Soc.* **1929**, *51*, 1436.

88. L. M. Branscomb, *Phys. Rev.* **1952**, *86*, 258.

89. T. Yu and M. C. Lin, *J. Am. Chem. Soc.* **1993**, *115*, 4371.

90. A. A. Ruth, E. -K. Kim, and A. Hese, *Phys. Chem. Chem. Phys.* **1999**, *1*, 5121.

91. T. Suzuki and M. Ito, *J. Phys. Chem.* **1987**, *91*, 3537.

92. D. Romanini, L. Biennier, F. Salama, A Kachanov, L. J. Allamandola, and F. Stoeckel, *Chem. Phys. Lett.* **1999**, *303*, 165.

93. F. Salama and L. J. Allamandola, *J. Chem. Phys.* **1991**, *94*, 6964.

94. T. Pino, N. Boudin, and P. Bréchignac, *J. Chem. Phys.* **1999**, *111*, 7337.

95. G. D. Schmidt, M. Cohen, and B. Margon, *Astrophys.*, **1980**, *239*, L133.

96. R. F. Warren-Smith, S. M. Scarrott, and P. Murdin, *Nature*, **1981**, *292*, 317.

97. G. D. Schmidt and A. N. Witt, *Astrophys. J.*, **1991**, *383*, 698.

98. S. M. Scarrott, S. Watkins, J. R. Miles, and P. J. Sarre, *Mon. Not. R. Astrom. Soc.*, **1992**, *255*, 11P.

99. P. J. Sarre, J. R. Miles, and S. M Scarrott, *Science*, **1995**, *269*, 674.

100. P. J. Sarre, *et al.*, *Mon. Not. R. Astrom. Soc.*, **1995**, *277*, L41.

101. R. J. Glinski and J. A. Nuth, *Astrophys. Space Sci.*, **1997**, *249*, 143.

102. S. J. Fossey, *Nature*, **1991**, *353*, 393.

103. P. J. Sarre, *Nature*, **1991**, *351*, 356.

104. W. Weltner Jr. and D. McLeod Jr., *J. Chem. Phys.*, **1964**, *40*, 1305.

105. V. E. Bondybey and J. H. English, *J. Chem. Phys.*, **1978**, *68*, 4641.

106. J. Szczepanski and M . Vala, *J. Chem. Phys.*, **1993**, *99*, 7371.

107. S. P. McGlynn, T. Azumi, and M. Kinoshita, *Molecular Spectroscopy of the Triplet State*, Prentice-Hall, Inc.: Englewood Cliffs, **1969**.

108. J. Szczepanski, S. Eckern and M . Vala, *J. Phys. Chem.*, **1995**, *99*, 8002.

109. M. Dibben, J. Szczepanski, C. Wehlburg, and M . Vala, *J. Phys. Chem.*, **2000**, *104*, 3584.

110. D. E. Powers, S. G. Hansen, M. E. Geusic, A. C. Pulu, J. B. Hopkins, T. G. Dietz, M. A. Duncan, P. R. R. Langridge-Smith, and R. E. Smalley, *J. Phys. Chem.*, **1982**, *86*, 2556.

111. K. Pitzer and E. Clementi, *J. Am. Chem. Soc.*, **1959**, *81*, 4477.

BIOGRAPHICAL SKETCH

Jason Frank Fuller was born June 9, 1974, in Natchez, Mississippi. Jason lived in Natchez until he graduated from Natchez High School in 1992. He continued his education at Mississippi College in Clinton, Mississippi, graduating with a Bachelor of Science degree in chemistry in 1996. During his studies at Mississippi College, Jason began his research career with Dr. Edward Valente, working in synthetic organic chemistry, specializing in crystal structure determinations. Jason continued his research career at the University of Florida in 1996, receiving his Ph.D. in 2001. While at the University of Florida Jason worked with the Vala research group.

I certify that I have read this study and that in my opinion it conforms to acceptable standards of scholarly presentation and is fully adequate, in scope and quality, as a dissertation for the degree of Doctor of Philosophy.

Martin T. Vala, Chair
Department of Chemistry

I certify that I have read this study and that in my opinion it conforms to acceptable standards of scholarly presentation and is fully adequate, in scope and quality, as a dissertation for the degree of Doctor of Philosophy.

William Weltner, Jr.
Professor of Chemistry

I certify that I have read this study and that in my opinion it conforms to acceptable standards of scholarly presentation and is fully adequate, in scope and quality, as a dissertation for the degree of Doctor of Philosophy.

John R. Eyler
Professor of Chemistry

I certify that I have read this study and that in my opinion it conforms to acceptable standards of scholarly presentation and is fully adequate, in scope and quality, as a dissertation for the degree of Doctor of Philosophy.

John A. Zoltewicz
Professor of Chemistry

I certify that I have read this study and that in my opinion it conforms to acceptable standards of scholarly presentation and is fully adequate, in scope and quality, as a dissertation for the degree of Doctor of Philosophy.

Charles M. Telesco
Professor of Astronomy

This dissertation was submitted to the Graduate Faculty of the Department of Chemistry in the College of Liberal Arts and Sciences and to the Graduate School and was accepted as partial fulfillment of the requirements for the degree of Doctor of Philosophy.

August 2001

Dean, Graduate School